Effects of contact materials on friction damping performance

by

Kevin Bruggeman

to obtain the degree of Master of Science
at the Delft University of Technology,
to be defended publicly on Tuesday February 28, 2023 at 2:00 PM.

Student number:	4724097	
Project duration:	April 1, 2022 – February 28, 2023	
Thesis committee:	Dr. A. Cicirello,	TU Delft, chair
	Dr. L. Marino,	TU Delft, daily supervisor
	Dr. ir. K. N. van Dalen,	TU Delft
	Dr. A. Cabboi,	TU Delft

Style: TU Delft Report Style, with modifications by Daan Zwaneveld

TU Delft

Preface

This master thesis report is submitted to obtain the degree of Master of Science at the Delft University of Technology. The research of this thesis was performed between April 2022 and February 2023 at the Faculty of Civil Engineering and Geo-sciences, under the Section of Mechanics and Physics of Structures in the Department of Engineering Structures. To the best of my knowledge, the work described in this thesis report is original, except where due reference has been made to acknowledge the work of others.

I would like to sincerely thank my thesis committee, consisting of Alice Cicirello, Luca Marino, Alessandro Cabboi and Karel van Dalen, for the feedback and advices they gave me during the progress meetings of this project. Secondly, I would like to express my gratitude towards my daily supervisor Luca Marino for his immensely helpful guidance and support. The many discussions we had greatly improved the quality of this study and I am thankful for the lessons they taught me, which I am sure will be useful in my career.

Last but not least, I would like to thank my loving girlfriend and my family. Their encouragement and support helped me very much during my years of study at the Delft University of Technology.

Kevin Bruggeman
Hoogerheide, the Netherlands, February 2023

Abstract

Friction damping is common in engineering structures for the purpose of energy dissipation and vibration control. Examples of applications are bolted connections and earthquake isolation systems. However, there is a shortage of works that investigate the effects of different contact materials on the energy dissipation performance and friction behaviour of friction dampers, which is valuable knowledge for design optimization.

This thesis uses a numerical approach to explore the time response and energy dissipated by friction of the harmonically excited SDOF (single-degree-of-freedom) system with Coulomb friction contact between the sliding mass and a fixed wall. In addition, for the same SDOF system, an experimental investigation of the friction damping performance in terms of friction behaviour and energy dissipation is carried out for (1) steel, (2) rubber and (3) aramid contact materials. The aim is to get a better understanding of how different contact materials affect the performance of friction dampers. Various time scales, excitation frequencies and friction forces are considered.

The main findings of this research are: (1) the characterization of the friction behaviour of steel-to-steel, rubber-to-steel and aramid-to-steel contacts; (2) the comparative analysis of the energy dissipation performance of the different contact materials; (3) the assessment of the long-term performance of the different contacts; (4) the comparison between numerical results based on the Coulomb friction model and experimental results. The tests have shown that rubber has the highest energy dissipation capacity and fairly unstable behaviour, steel has the second highest energy dissipation and irregular behaviour and aramid has the lowest energy dissipation performance and very consistent behaviour. Finally, the application of a method that calculates the energy dissipation of friction damping based on direct experimental outputs is an important contribution to the field regarding experimental investigations.

Contents

List of Figures

1
Introduction

Contents

1.1. Friction damping and applications in engineering structures

Friction forces as a result of static or dynamic loading are extremely common in many types of engineering structures. Friction can lead to negative effects such as abrasion, cracking and fatigue [1], structural damage and even failure, reduction of damping and noise pollution. These consequences are very disadvantageous to engineering structures and their performance.

On the other hand, friction can also positively affect the performance of various types of engineering structures. It is used to facilitate vibration reduction, vibration isolation and energy dissipation [2–7]. Energy dissipation and subsequent vibration control can be achieved through friction damping, which is prevalent in many different engineering fields, such as robotics, turbomachinery and civil engineering. Friction damping can be directly added to a structure, for example in the form of friction dampers, or can be an additional property of for example bolted connections and truss and brace frames, which have a lot of friction joints. Friction dampers are devices that dissipate energy by using dry friction [2]. They are very popular for the purpose of seismic isolation and fortification because their performance is unaffected by the amplitude and frequency of loading and the number of loading cycles.

Moreover, they are versatile, simple and reliable to use and have a relatively high energy dissipation capacity due to their rectangular hysteresis loops [2, 5]. A large amount of novel friction dampers have been invented and applied in the field of civil engineering since 1980 [5]. Friction dampers are also applied in suspension systems and robotic machines [2].

Even though friction is an effective type of damping and common in engineering structures, the current knowledge of the effects of friction on the dynamic response of mechanical systems is limited. According to Marino et al. [2, 4, 8], the main challenges in the development of a thorough understanding of friction damped systems are caused by: the unrepeatable nature of friction processes, the nonlinearity of dynamic friction forces and the absence of a universal and predictive friction model. In addition, there are various conditions affecting the properties of a friction contact, like humidity, cleaning and polishing of the surface and temperature. Several long-term effects that change the properties of the contact, such as wear and the formation of debris, are caused by friction during sliding. Due to all these factors playing a role in the friction process, it is difficult to reproduce experimental results and predict the performance of friction dampers via experiments [2, 3].

1.2. Energy dissipation by friction and contact materials

Friction is a highly complex physical process and is difficult to reliably investigate through experiments, as mentioned in Section 1.1. However, it is still a popular research subject. There is an abundance of theoretical work on friction, which mainly deploy analytical and numerical methods to attain results. Asymmetric and sub-harmonic resonant solutions of a harmonically excited dry friction oscillator have been studied in references [9, 10], illustrating interesting features of the asymmetric responses. Marino et al. have investigated the dynamic response of a SDOF system with Coulomb friction contact subjected to harmonic base excitation for a fixed wall and base-wall configuration, both numerically and experimentally [2, 4, 8]. Similar analytical results for the fixed wall case were found by Riddoch et al. [11].

Research on the subject of energy dissipation and friction damping has been performed as well. In reference [12], beam-to-column joints equipped with friction dampers have been developed and tested for various materials in the friction contact. The results are compared in terms of hysteresis cycles and energy dissipation. The main findings of this work are that the steel-to-steel contact depicted quite unstable behaviour and the hard-rubber-to-steel contact showed very stable behaviour and high energy dissipation capacity. Anoushehei et al. investigated the behaviour of a rotational friction damper under cyclic loading for different metal friction pads [6]. They found that the surfaces of the aluminum, galvanized steel and steel pads show extensive wear after cyclic loading, whereas stainless steel is only damaged marginally. The study in [7] shows that the Coulomb friction model is accurate enough to predict the maximum energy dissipation of a friction damper with stiff localized contacts and large relative displacements in the contact, through means of numerical calculations and experiments. Finally, reference [13] uses vibration transmission and energy flow characteristics to analytically determine the energy dissipation of a SDOF dynamical system with Coulomb friction. It is found that the friction contact can effectively suppress the vibration response and dissipate energy.

To the best of the author's knowledge, there is a lack of experimental studies on the effects of different contact materials on the energy dissipation by friction. Such works could be extremely useful for the optimization of friction dampers. The only work found carrying out such an investigation is reference [12]. Furthermore, knowledge on the long-term performance and abrasion resistance, frictional behaviour and the best fitting friction model of contact materials is limited. This research gap will be addressed in this thesis.

1.3. Aim, scope and methodology of the thesis

The study that is conducted in this thesis aims to give insight into the effects of different contact materials on the dynamic response and energy dissipation performance of friction damped mechanical systems.

To develop this understanding, assuming the harmonically excited SDOF system with Coulomb friction contact between a fixed wall and sliding mass for the sake of simplicity, the energy dissipation by friction and friction behaviour of the moving mass are investigated numerically and experimentally. The experiments consist of three contact configurations: a steel-to-steel contact, a rubber-to-steel contact and an aramid-to-steel contact. This allows for a comparison of the performance and behaviour of the different contact materials, those being (1) steel, (2) rubber and (3) aramid.

Based on the research gap described in Section 1.2, the following research questions are derived:

1. What kind of friction behaviour is induced by different contact materials?
2. What are the pros and cons of each material when comparing the energy dissipation performance?
3. How do the contact materials perform in the long term?

These research questions have been answered by completing the following tasks:

1. Deriving methods to calculate the energy dissipation by friction. These methods can be used on numerical and experimental time responses.
2. The implementation of a numerical algorithm that evaluates the time response of the harmonically excited SDOF system with Coulomb friction damping. Both continuous and stick-slip motions can be evaluated.
3. Obtaining numerical results for the time response and the energy dissipation of the harmonically excited SDOF system with Coulomb friction contact, for various friction forces and excitation frequencies.
4. Performing experiments for various frequencies and friction forces for the different friction contact configurations mentioned previously. One short time scale and one long time scale are considered. The test setup can be appropriately represented by a SDOF model. The measured experimental time responses are used to compute the energy dissipation and to analyze the friction behaviour. Afterwards, the numerical and experimental results are compared.

In addition to these tasks, the energy dissipation calculation method is validated by applying it to a harmonically excited SDOF system with viscous damping. Subsequently, the performance of the viscous damped system is compared to the performance of the Coulomb friction damped system.

1.4. Contributions

The work carried out in this thesis leads to the following two contributions to the field:

1. The development of a calculation method that evaluates the energy dissipation of a friction damper based on the harmonic excitation and mass response. Because these

two motions can be measured during experiments, this calculation method is suitable for experimental investigations.

2. A comparative analysis of the performance of three different contact materials, namely steel, rubber and aramid. The material performance is assessed based on the friction behaviour and energy dissipation capacity.

1.5. Structure of the thesis

This thesis report consists of six chapters. The required theoretical background on the Coulomb friction model and the fundamental analytical solution for the harmonically excited SDOF system with Coulomb friction is given in Chapter 2. The energy dissipation calculation methods are presented in this chapter as well. In Chapter 3, the numerical results for the friction behaviour and energy dissipation of the SDOF Coulomb friction damped system are shown. Following this, the experimental investigation of the friction behaviour and energy dissipation performance of the different contact materials is carried out in Chapter 4. Chapter 5 provides the most important conclusions of the thesis. Finally, Chapter 6 presents critical observations on the performed work and recommendations for further research.

2

Theoretical background

Contents

2.1. Introduction

The objective of this chapter is to present the theoretical background required for the numerical and experimental investigations carried out in the following chapters.

More specifically, the Coulomb friction model, which is the friction model considered in this thesis, is explained, as well as Den Hartog's fundamental analytical solution for the SDOF system with Coulomb friction contact under harmonic excitation. Because the metric used in this research for evaluating the dissipation performance is the energy dissipated by friction, several energy dissipation calculation methods are derived.

The Coulomb friction model is briefly described in Section 2.2. Afterwards, the exact solution for the harmonically excited SDOF system with Coulomb friction damping by Den Hartog is reviewed in Section 2.3. Lastly, the methods used to calculate the energy dissipation by friction are introduced in Section 2.4.

2.2. Coulomb friction model

In the field of mechanical systems involving friction, finding accurate models that correctly describe friction forces occurring in the contact between two bodies has always been a great challenge and popular research subject. Nowadays, numerous friction models exist and are still being developed. One of the most prevalent and simple friction models is the Coulomb friction model by Coulomb and Amontons, also known as the law of proportionality between friction force and normal force [14]:

$$F_f = \mu_d F_n \tag{2.1}$$

where F_f is the friction force, F_n is the normal force and μ_d is the kinetic friction coefficient which depends on the surface of the materials in the friction contact. The friction force in Equation 2.1 is generated by the sliding of two bodies in contact and is called the kinetic friction force.

Morin later extended the Coulomb model with static friction or stiction [15]. The static friction force is defined as the force that is needed to make a body slide across the surface of another body, starting from rest or static conditions. The static friction force is generally greater than the kinetic friction force [16]. The mathematical expression of the Coulomb friction model with stiction is as follows:

$$F_f = \begin{cases} \mu_d F_n & \text{if } \mathrm{v}_r < 0 \\ [-\mu_s F_n, \mu_s F_n] & \text{if } \mathrm{v}_r = 0 \\ -\mu_d F_n & \text{if } \mathrm{v}_r > 0 \end{cases} \tag{2.2}$$

Where μ_s is the static friction coefficient and v_r is the relative velocity between the sliding bodies whose surfaces are in contact.

The Coulomb model and Coulomb model with stiction are plotted in Figure 2.1, based on their mathematical force-velocity formulation described in Equation 2.1 and 2.2 respectively. It is evident that according to both variations of the Coulomb model, the friction force only changes when the velocity changes direction or becomes zero. The magnitude of the velocity has no effect on the friction force. In the following section the Coulomb friction model plays an important role in the work by Den Hartog.

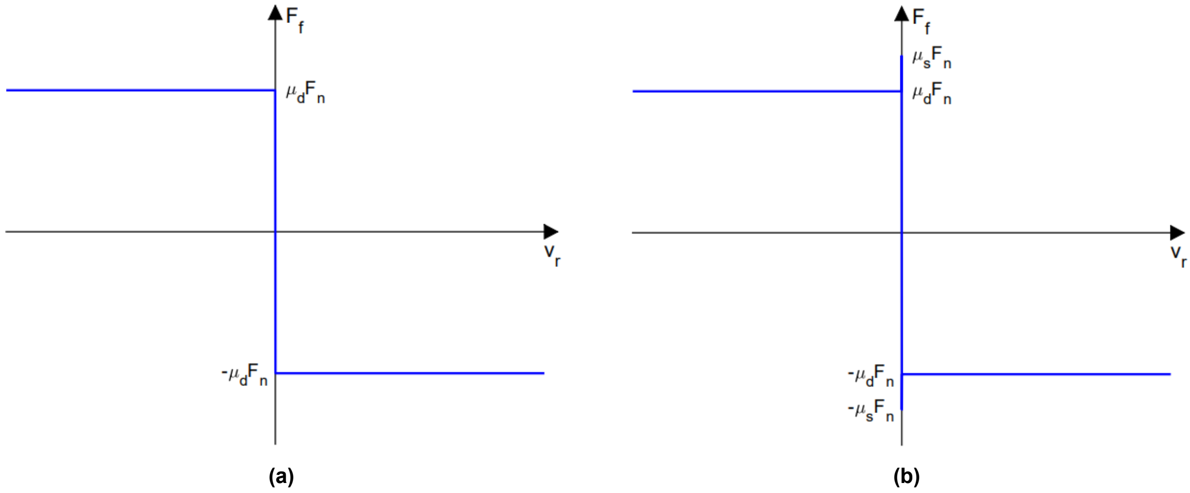

Figure 2.1: Coulomb friction model **(a)** and Coulomb friction model with stiction **(b)**, friction force versus the relative velocity between the two sliding bodies in contact [2].

2.3. Den Hartog's analytical solution for the SDOF system with Coulomb friction

Although the dynamic behaviour of friction damped systems is difficult to determine due to their nonlinear nature (a system is nonlinear when a change in input does not lead to a proportional change in output [2]), several analytical, semi-analytical and numerical time integration solution methods have been developed to analyze the dynamics of friction damped systems. One of the most important and influential studies regarding the analytical solution methods is the work by Den Hartog [17, 18]. He derived an analytical solution for the continuous steady-state motion of a harmonically excited SDOF system with Coulomb friction contact between the oscillating mass and a fixed wall. In this section, the solution by Den Hartog is briefly reviewed as it is essential for the investigations carried out in this thesis. This review is also based on Marino's work in reference [2].

The SDOF model with Coulomb friction contact in Figure 2.2 is introduced. It is a mass-spring system with mass m and spring stiffness k. The system is excited through the harmonic load $P\cos(\omega t)$, with amplitude P and frequency ω. The mass motion is denoted as x. The sliding mass is in contact with a fixed wall, generating a Coulomb friction force of amplitude F. It is worth mentioning that this system is equivalent to a harmonically base-excited system (instead of the harmonic load, the mass is excited by the harmonic motion of the base that the spring is connected to) with base motion $Y\cos(\omega t)$, with displacement amplitude Y and frequency ω, by replacing P in Figure 2.2 with kY. The governing equation of motion of the

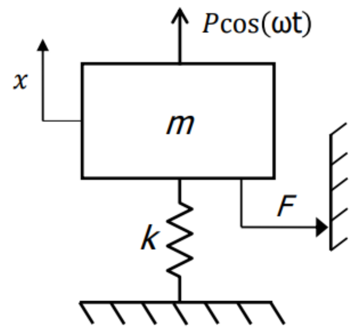

Figure 2.2: Harmonically excited SDOF system with Coulomb friction contact between a fixed wall and the mass [2].

SDOF system in Figure 2.2 is:

$$m\ddot{x} + kx + F\text{sgn}(\dot{x}) = P\cos(\omega) \tag{2.3}$$

With the signum function sgn() being defined as follows:

$$\text{sgn}(\dot{x}) = \begin{cases} -1 & \text{if } \dot{x} < 0 \\ [-\mu, \mu] & \text{if } \dot{x} = 0 \\ 1 & \text{if } \dot{x} > 0 \end{cases} \tag{2.4}$$

With μ being the ratio between the static and kinetic friction force. In case that the mass is stationary and thus $\dot{x} = 0$, the value of the signum function in the range $[-\mu, \mu]$ is such that the friction force is in equilibrium with the excitation force so that the net force is zero. Stiction is not taken into account by Den Hartog, so throughout this thesis $\mu = 1$ is assumed.

The governing Equation 2.3 needs to be made non-dimensional in order to reduce the number of parameters. To be able to do this, the dimensionless time is considered:

$$\tau = \omega t \tag{2.5}$$

With t being standard dimensional time. The dimensionless mass displacement is introduced as well:

$$\bar{x} = \frac{x}{P/k} \tag{2.6}$$

In addition, two non-dimensional parameters are presented. These are the frequency ratio, the ratio between the driving frequency and natural frequency of the system:

$$r = \frac{\omega}{\omega_n} = \omega\sqrt{\frac{m}{k}} \tag{2.7}$$

With ω_n being the natural frequency, and the friction ratio, the ratio between the amplitudes of the friction force and the harmonic load:

$$\beta = \frac{F}{P} \tag{2.8}$$

After plugging Equation 2.5 and 2.6 into the governing Equation 2.3, dividing by P and using the two newly introduced parameters in Equation 2.7 and 2.8, the non-dimensional governing equation is acquired:

$$r^2\bar{x}'' + \bar{x} + \beta \text{sgn}(\bar{x}') = \cos(\tau) \tag{2.9}$$

Den Hartog made several important assumptions: (1) the time response of the mass is continuous (there are no stops), (2) a steady-state motion has been reached, (3) the response period equals the excitation period (which is 2π in dimensionless form) and (4) the response is anti-periodic (a special form of symmetry, the second half of the response equals the negative of the first half). Under these assumptions and after imposing boundary conditions of the half-period, Den Hartog derived an exact solution of the dimensionless mass motion in the dimensionless half-period [0,π]:

$$\bar{x} = \overline{X}\cos(\tau) + \beta U \sin(\tau) + \beta\left[1 - \cos\left(\frac{\tau}{r}\right) - Ur\sin\left(\frac{\tau}{r}\right)\right] \tag{2.10}$$

Where $\overline{X}$ is the non-dimensional amplitude of the mass motion, which can be calculated as:

$$\overline{X} = \sqrt{V^2 - (\beta U)^2} \tag{2.11}$$

With V and U being the response function of an undamped SDOF system and the damping function, respectively:

$$V = \frac{1}{1 - r^2} \tag{2.12}$$

and:

$$U = \frac{\sin(\frac{\pi}{r})}{r[1 + \cos(\frac{\pi}{r})]} \tag{2.13}$$

Finally, the phase angle between the excitation and time response of the mass can be computed with the following two formulas:

$$\cos(\phi) = \frac{\overline{X}}{V} \qquad \text{and} \qquad \sin(\phi) = -\frac{\beta U}{V} \tag{2.14}$$

The solution by Den Hartog presented in this section is fundamental in the field of mathematical analysis of friction damped systems and is used in the next section to obtain methods for calculating the energy dissipated by friction. From this point forward, the main SDOF Coulomb friction damped system considered in this thesis is the harmonically base-excited case, since this model represents the used experimental setup most accurately. All expressions given above are also valid for this system by substituting P with kY, as mentioned previously for Figure 2.2.

2.4. Energy dissipation calculation methods

The friction contact in the harmonically base-excited SDOF system provides damping through the dissipation of energy. The main complication in the calculation of the energy dissipated by friction during experiments is that the friction force cannot be measured directly. Obtaining the work done by the friction force is thus impossible. A solution that does not require the friction force is found and subsequently three energy dissipation calculation methods are developed. These methods are: the energy input method, the hysteresis method and the analytical method. The different methods are explained in what follows. It is worth noting that the Coulomb friction model can be used to accurately determine the energy dissipated by friction, according to [7].

2.4.1. Energy input method

Steady-state conditions are assumed, so the amplitude of the response is constant. This in turn means that the total energy in the system at the start and end of each response cycle is the same, because if the energy would change, the amplitude would change as well. The energy input per cycle must then be equal to the the energy dissipated per cycle by friction damping [19]. The energy input is the work done by the excitation force per cycle, and this force can be measured during tests.

The energy input by the base excitation force per cycle can be evaluated as:

$$\Delta E_{in} = \int_{T} kY \cos(\omega t)\dot{x}\, dt \tag{2.15}$$

With ΔE_{in} being the energy input per cycle, $\dot{x}$ being the mass velocity and T being the time duration of one cycle. To reduce the number of parameters, the non-dimensional form can be obtained by substituting the non-dimensional time and displacement from Equation 2.5 and 2.6 (replacing P with kY) into Equation 2.15 and dividing by kY^2:

$$\Delta\overline{E}_{in} = \Delta\overline{E}_{fric} = \int_{2\pi} \bar{x}' \cos(\tau)\, d\tau \tag{2.16}$$

With $\Delta\overline{E}_{in}$ representing the non-dimensional energy input per cycle, $\Delta\overline{E}_{fric}$ representing the non-dimensional energy dissipated by friction per cycle, 2π representing the length of one dimensionless time period and $\bar{x}'$ representing the dimensionless mass velocity. The units check out, since the expression was divided by kY^2, and the unit of kY^2 is Newton meter or Joule, which is the unit of energy. The friction energy dissipation per cycle can thus be calculated with Equation 2.16. However, because the mass velocity $\bar{x}'$ is hard to measure during experiments and numerical differentiation of displacement measurements is not accurate enough, the method needs to be adapted in order to be able to use it for experiments.

2.4.2. Hysteresis method

By using the following identity:

$$\bar{x}' = \frac{d\bar{x}}{d\tau} \tag{2.17}$$

The energy input method shown in Equation 2.16 can be rewritten as follows:

$$\Delta\overline{E}_{fric} = \int_{C} \cos(\tau)\, d\bar{x} \tag{2.18}$$

With C meaning one cycle of the mass motion $\bar{x}$. Since cos(τ) is the forcing of the system and $\bar{x}$ the displacement of the mass, Equation 2.18 is the area inside the hysteresis loop of one steady-state response cycle. Literature confirms that this area equals the energy dissipation by Coulomb friction [19]. This calculation method is very easy to apply because it only requires the mass and base motion, two displacements which can be measured during experiments or are direct outputs of numerical simulations. This is a significant advantage of the hysteresis method and it is therefore preferred over the energy input method.

2.4.3. Analytical method

To allow for a verification of the hysteresis method, which will be used in the experimental investigation of this thesis, the analytical energy dissipation calculation method is developed. It is based on Den Hartog's solution explained in Section 2.3 and thus is only valid in the continuous motion regime. The exact solution by Den Hartog incorporates the lag between excitation and response through the phase ϕ, meaning that Equation 2.16 can be rewritten as:

$$\Delta\overline{E}_{fric} = \int_0^{2\pi} \bar{x}' \cos(\tau + \phi)\, d\tau \tag{2.19}$$

The integration bounds are 0 and 2π so one period is considered. Den Hartog's assumptions mentioned in Section 2.3 apply again. Since the response is anti-periodic, the velocity $\bar{x}'$, which is the derivative of the response, is anti-periodic as well. This means that the integration bounds can be changed:

$$\Delta\overline{E}_{fric} = 2\int_0^{\pi} \bar{x}' \cos(\tau + \phi)\, d\tau \tag{2.20}$$

Applying the trigonometric identity $\cos(a+b) = \cos(a)\cos(b) - \sin(a)\sin(b)$, Equation 2.20 becomes:

$$\Delta\overline{E}_{fric} = 2\int_0^{\pi} \bar{x}'[\cos(\tau)\cos(\phi) - \sin(\tau)\sin(\phi)]\, d\tau \tag{2.21}$$

Differentiating the mass motion for the time interval $[0, \pi]$ in Equation 2.10 with respect to τ, gives the analytical expression of the velocity:

$$\bar{x}' = -\overline{X}\sin(\tau) + \beta U \cos(\tau) + \frac{\beta}{r}\sin\left(\frac{\tau}{r}\right) - \beta U \cos\left(\frac{\tau}{r}\right) \tag{2.22}$$

Plugging Equation 2.22, 2.14 (phase angle), 2.12 (response function) and 2.13 (damping function) into Equation 2.21 and simplifying finally gives the following expression for the analytical energy dissipation:

$$\Delta\overline{E}_{fric} = 4\beta\overline{X} \tag{2.23}$$

Literature proposes the use of equivalent viscous damping for Coulomb friction to calculate the energy dissipated per cycle. The dimensional energy dissipation according to literature is $4FX$, with F being the amplitude of the friction force and X being the amplitude of the mass motion [19, 20]. This corresponds flawlessly with the non-dimensional analytical method in Equation 2.23.

2.5. Conclusion

This chapter has provided the necessary prerequisite knowledge for the analyses performed in this thesis.

The Coulomb friction model, with and without stiction, has been discussed. Secondly, the analytical solution for the continuous steady-state response of a harmonically excited SDOF system with Coulomb friction derived by Den Hartog has been shown. Three methods for the calculation of the energy dissipation by friction have been developed as well.

The most important outcome of this chapter is the hysteresis method which can be used to evaluate the energy dissipation, both numerically and experimentally. This method can be verified with the analytical method. These two dissipation calculation methods, together with the governing equation of the SDOF system with Coulomb friction, will be used in the next chapters of this report.

3

Numerical investigation of a Coulomb friction damped system

Contents

3.1. Introduction

This chapter carries out a numerical investigation of the steady-state time response and the energy dissipated by friction per steady-state cycle of the harmonically excited SDOF mass-spring system with Coulomb friction contact. The aim of this investigation is to provide a numerical framework and validation for the experimental results that will be discussed in the following chapter. Additionally, the goal is to gain insight into the friction behaviour and energy dissipation performance and how these two properties depend on the excitation frequency and friction force.

An algorithm that computes the time response of the dynamic system through numerical integration is implemented, handling both continuous and stick-slip motion regimes. Numerical time responses are evaluated for varying frequencies and friction forces to acquire a large data set. Afterwards, the friction energy dissipation of these numerical simulations is calculated with the analytical and hysteresis method introduced in the previous chapter and the results are compared. The hysteresis method is validated by applying it to the harmonically excited SDOF mass-spring-dashpot system.

Section 3.2 discusses the solution method of numerical time integration and its problems and limitations. The implemented numerical algorithm is explained in detail in Section 3.3. The obtained numerical results, being the steady-state time response and the energy dissipation of the system for both continuous and stick-slip motion, are presented in Section 3.4. Based on these results, a detailed discussion of the friction and energy dissipation behaviour is given. Lastly, Section 3.5 presents a SDOF viscous damped system to validate the hysteresis method and compares the energy dissipation performance of the viscous damped system to the performance of the Coulomb friction damped system.

3.2. Numerical time integration

As mentioned in Section 2.3, one method to examine the dynamic behaviour of friction damped mechanical systems is numerical time integration. This solution method will be used to solve the governing equation of motion in Equation 2.9 of the SDOF model with Coulomb friction in Figure 2.2.

The high nonlinearity of the Coulomb friction model, which is due to the discontinuity at zero velocity where the friction force changes direction, causes some difficulty for the numerical time integration approach. Furthermore, in the stick-slip motion regime, the transition between sticking and sliding of the mass (zero and non-zero velocity) occurs very quickly and frequently. In the case of a numerical solver with automatic step size, these numerous switches between sticking and sliding phases drastically increase computation time. Numerical solvers with fixed step size do not suffer from high computation times but lack accuracy [3]. This problem regarding the discontinuities and swift changes between sticking and sliding phases is called numerical stiffness. A simple technique to handle stiffness is applying an event-driven approach that incorporates standard numerical integration methods. The event function stops the integration sequence whenever the mass gets stuck and imposes new initial conditions for the next integration sequence [8]. The implemented numerical algorithm explained in the next section is also event-driven.

The numerical time integration also covers the transient phase of the response of the SDOF model with Coulomb friction contact. Since only the steady-state response is of importance in this thesis, this increases computation time. This especially holds for low friction cases, which are lightly-damped and thus have a long transient [3]. However, both high and low friction systems will be explored in the numerical analysis, so the high computational costs are accepted.

Numerical solutions are dependent on and limited by the friction model that is used. Even though the Coulomb friction model is relatively simple, more advanced friction models have their own limitations as well. In order to get a thorough and more complete understanding of the dynamic behaviour of friction damped SDOF systems and their dissipative properties, experimental results will be compared to and validated with numerical results based on the Coulomb friction model.

3.3. Explanation of the algorithm

The aim of the implemented algorithm is to compute the time response of the SDOF Coulomb friction damped system for a specific combination of frequency and friction ratio. Subsequently, the energy dissipated per cycle by friction for this combination of r and β values can be calculated with the energy dissipation calculation methods from Section 2.4.

The governing equation in Equation 2.9 is numerically integrated to find the solution. Whereas continuous motions can be calculated with standard numerical integration methods, stick-slip motions entail the problem of numerical stiffness, as explained in Section 3.2. An event-driven approach is used to deal with this numerical stiffness. The algorithm uses a standard numerical integration method and the event handles the transition between sliding and sticking phases when certain imposed conditions are met. The numerical algorithm is visualized in a flowchart in Figure 3.1 and the steps are explained below.

1. The time response of the SDOF system is fully governed by the frequency ratio r, friction ratio β and the ratio between the static and kinetic friction force μ, three dimensionless parameters introduced in Section 2.3. These parameters, together with the initial non-dimensional displacement $\bar{x}_0$, initial non-dimensional velocity $\bar{x}'_0$ and the amount of excitation periods N_{cyc}, are the input of the algorithm. Because dimensionless time is considered, the duration of each cycle is 2π. The final time of the numerical integration τ_f then equals

$2\pi N_{cyc}$. Different frequency and friction ratios are investigated. As mentioned in Section 2.2, it is assumed that $\mu = 1$. To make sure that a steady-state condition has been reached, $N_{cyc} = 100$. The initial displacement and velocity have been set to zero.

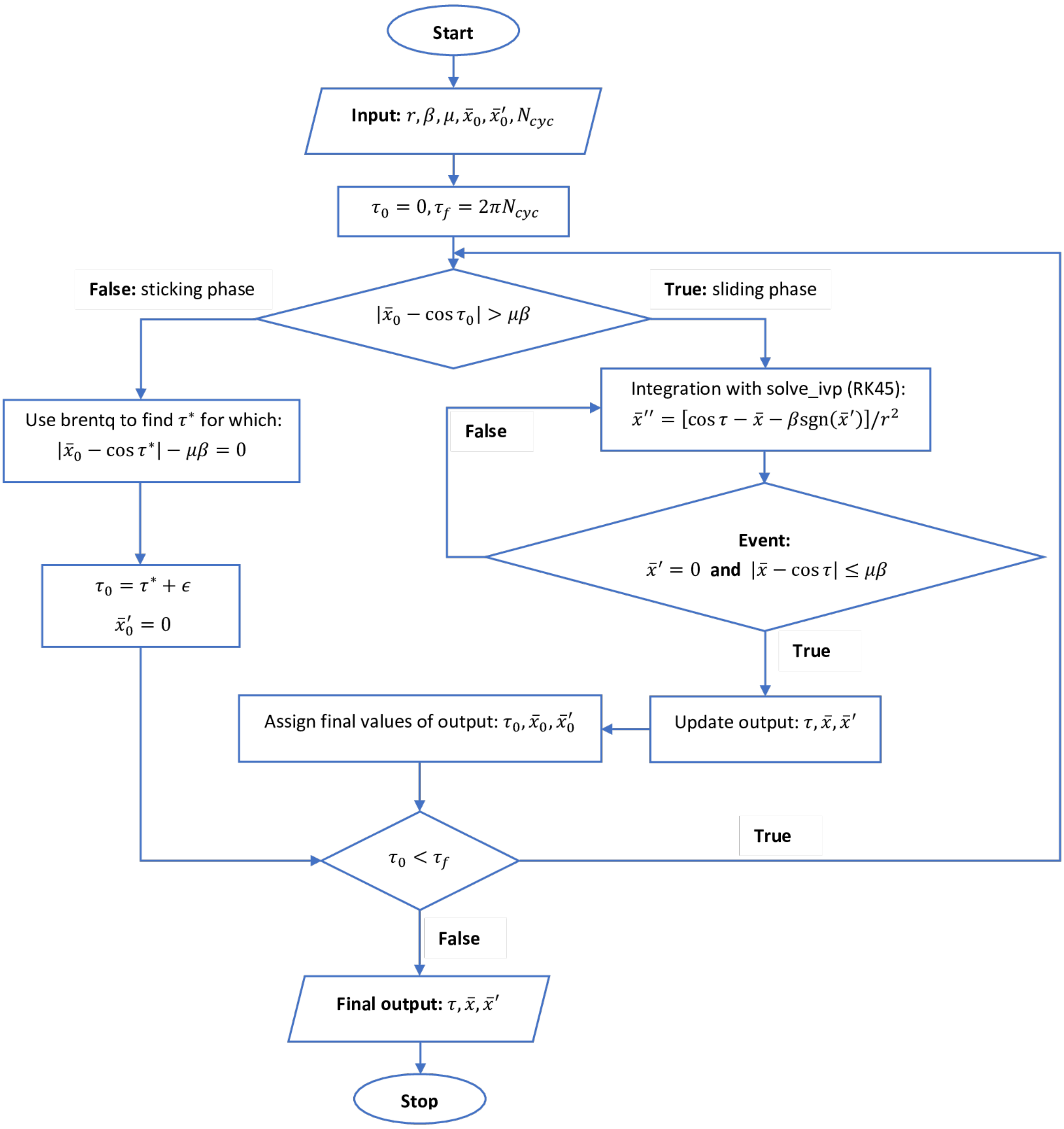

Figure 3.1: Flowchart of the algorithm that computes the time response of the harmonically excited SDOF system with Coulomb friction contact via numerical integration. Based on flowchart by Marino [2].

2. Given the initial conditions, it is first verified if the excitation force overcomes the maximum friction force with the equation:

$$|\bar{x}_0 - \cos\tau_0| > \mu\beta \tag{3.1}$$

The force on the left-hand side is the amplitude of the sum of all the non-inertial forces (including spring force and external excitation) acting in the frictional contact, the right-hand side is the friction force [8]. Based on which force is greater, the sticking or sliding phase will begin.

3. When the sliding phase takes place, there is no numerical stiffness since the motion is continuous. The governing equation of the SDOF system with Coulomb friction is integrated with the standard variable step numerical integration method Runge-Kutta, RK45 for short. This method is supported by Python in the numerical solver function solve_ivp from the Scipy package [21]. The integration is terminated if both event conditions are met. These conditions are $\bar{x}'_0 = 0$ (velocity of the mass is zero) and, similar to Equation (3.1), $|\bar{x}_0 - \cos\tau_0| \leq \mu\beta$ (excitation force is smaller than or equal to friction force). When the event conditions are simultaneously satisfied, the mass is stuck. The algorithm output, being (dimensionless) vectors of time, displacement and velocity, is updated and the last entries of these vectors become the new initial conditions. If the final time has not been reached yet, the algorithm goes back to step 1 and enters the sticking phase.

4. If sticking of the mass occurs, the next point in time where the dynamic loading in the contact overcomes the static friction force needs to be found. This is done by solving the below equation with the Brent root-finding algorithm [22] implemented in the Python function brentq from the Scipy package [21]:

$$|\bar{x}_0 - \cos\tau^*| - \mu\beta = 0 \tag{3.2}$$

After the time τ^* where the mass gets unstuck is obtained, the initial conditions for the next integration sequence are updated. The initial displacement stays the same and the initial velocity becomes zero because the mass was stuck and thus stationary. The new initial time becomes $\tau^* + \epsilon$. A very small margin of ϵ is added so that the event does not immediately terminate the next integration. When $\tau_0 < \tau_f$, the numerical algorithm goes back to the start and enters the sliding phase. Eventually the full numerical solution is calculated through piecewise integration of the continuous motion parts.

5. When the final time is reached, the algorithm has completed the numerical integration and returns the full output, being the time, displacement and velocity vectors.

3.4. Results and discussion

To directly obtain the time response of the SDOF system with Coulomb friction, the dimensionless displacement and time vectors of the numerical solution can be plotted against each other. The analytical method and hysteresis method from Section 2.4 are used to obtain the desired energy dissipation metrics from the numerical solution. This procedure is carried out for different combinations of the r and β parameters.

3.4.1. Steady-state time response

To gain insight into the different motion regimes and corresponding characteristics, time frames of the steady-state time response of several combinations of r and β are displayed in Figure 3.2. Each plot shows a different motion regime.

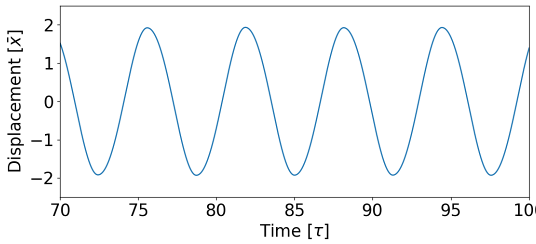

(a) Continuous motion, $r = 0.7$, $\beta = 0.2$

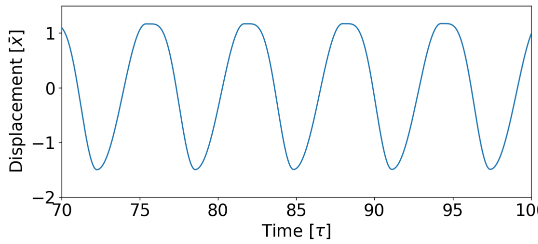

(b) Asymmetric non-sticking motion, $r = 0.5$, $\beta = 0.2$

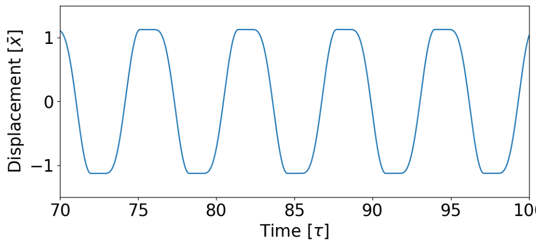

(c) Two-stops stick-slip motion, $r = 0.4$, $\beta = 0.3$

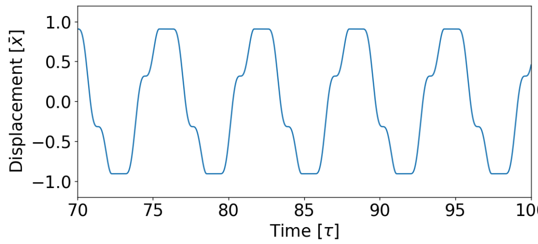

(d) Four-stops stick-slip motion, $r = 0.2$, $\beta = 0.3$

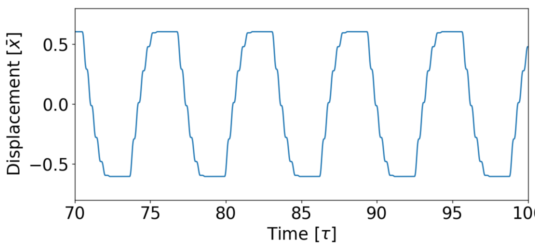

(e) Multiple-stops stick-slip motion, $r = 0.05$, $\beta = 0.4$

Figure 3.2: Short time frame of the steady-state time response of the SDOF system with Coulomb friction for various values of r and β, based on numerical results.

The observed numerical solutions are in good agreement with numerical results obtained by Marino [8] and analytical results by Riddoch et al. [11] for the same SDOF dynamic system. As can be seen in Figure 3.2, the amount of stops during one cycle of stick-slip motion increases with the friction ratio and decreases with the frequency ratio. The more stops a cycle has, the steeper and shorter these stops are. The amplitude of the mass displacement on the other hand decreases with friction and increases with frequency.

In addition, an asymmetric non-sticking time response is shown in Figure 3.2b (even though the positive peaks seem flat, these are not stops). This is an interesting phenomenon since all the other responses in Figure 3.2 are symmetric, which is expected because the sinusoidal excitation is symmetric as well.

Current knowledge on asymmetric behaviour is limited to theoretical studies from a mathematical perspective. Considering an equivalent SDOF system with Coulomb friction for numerical analysis, Licskó discussed asymmetric solutions [10] and Csernák et al. even found asymmetric non-sticking responses similar to Figure 3.2b for $\mu = 1$ [9]. These asymmetric non-sticking solutions exist for the even sub-resonant frequencies when:

$$r = \frac{1}{2n} \quad \text{and} \quad \beta \leq \frac{1}{4n^2 - 1} \tag{3.3}$$

where $n = 1, 2, 3, \dots$. The parameters of the asymmetric non-sticking solution in Figure 3.2b satisfy Equation 3.3, because $r = 0.5$ means that $n = 1$ and $\beta = 0.2 < \frac{1}{3}$.

3.4.2. Energy dissipation continuous motion

The energy dissipation per cycle of the numerical solutions is calculated with the analytical method (Equation 2.23) and the hysteresis method (Equation 2.18). The results of these two methods are compared as well. Since the analytical formula is only valid in the continuous motion regime, only continuous motions are considered.

Two hysteresis loops are illustrated in Figure 3.3 to better explain the application of the hysteresis method. As the forcing or excitation $\bar{y}$ is plotted against the displacement $\bar{x}$, the area inside this closed loop equals the non-dimensional energy dissipated by friction per cycle [19]. The two-stop hysteresis loop clearly has a different shape than the continuous one. For each numerical time response, one steady-state cycle can be assessed to determine the

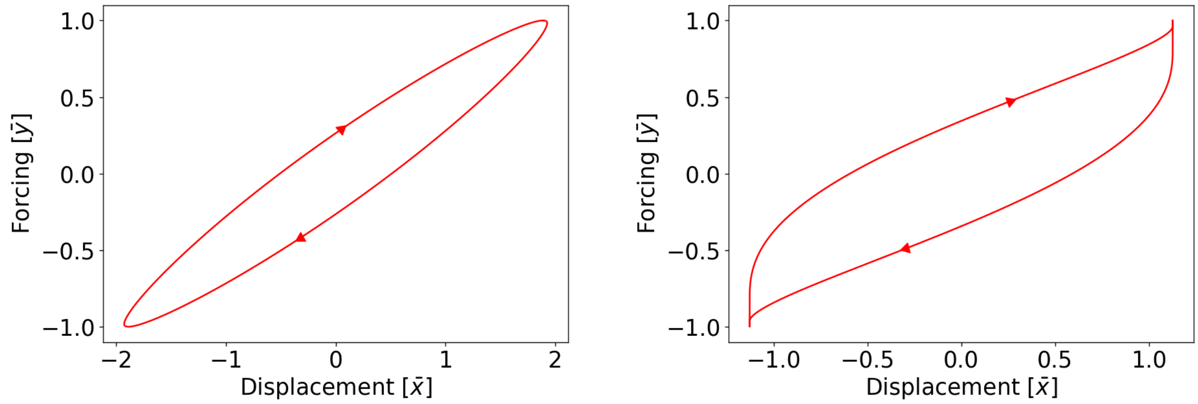

(a) Continuous motion, $r = 0.7$, $\beta = 0.2$ **(b)** Two-stops stick-slip motion, $r = 0.4$, $\beta = 0.3$

Figure 3.3: Hysteresis loop of one steady-state cycle of the SDOF Coulomb friction damped system for two different motion regimes, based on numerical results. The red arrows denote the flow direction of the loop.

energy dissipation.

Friction ratio values ranging from 0.1 to 0.8 ($\beta = 0.9$ causes only stick-slip) and the according frequency ratios for continuous motion are investigated. The limit values of r for continuous motion for each β are calculated according to Marino [4], who derived expressions for the boundary between stick-slip and continuous regimes for the SDOF system with Coulomb friction contact based on Den Hartog's work [17, 18]. The energy dissipation computed from the numerical solutions has been plotted in Figure 3.4. Because only the continuous regime is considered, the curves have different start and end points. An excellent agreement between the analytical and hysteresis energy dissipation calculation methods has been observed across the entire parameter space. Other noticeable things are:

- The energy dissipation peak is at resonance. This is logical since the dynamic system absorbs more energy the closer the excitation frequency is to its natural frequency.
- As expected, the higher the friction ratio and thus the friction force, the higher the energy dissipation. This makes sense because greater forces result in more work done per cycle. However, this principle only holds in general, since there are some exceptions for $\beta = 0.8$ and $r > 1$.
- With higher friction, the energy dissipation curve shifts slightly towards the left of the frequency range, similar to the dynamic magnification factor of SDOF systems with viscous damping [23]. For a sufficiently high damping ratio ζ, the damped natural frequency $\omega_d = \omega_n\sqrt{1-\zeta^2}$ is significantly lower than the undamped natural frequency ω_n and

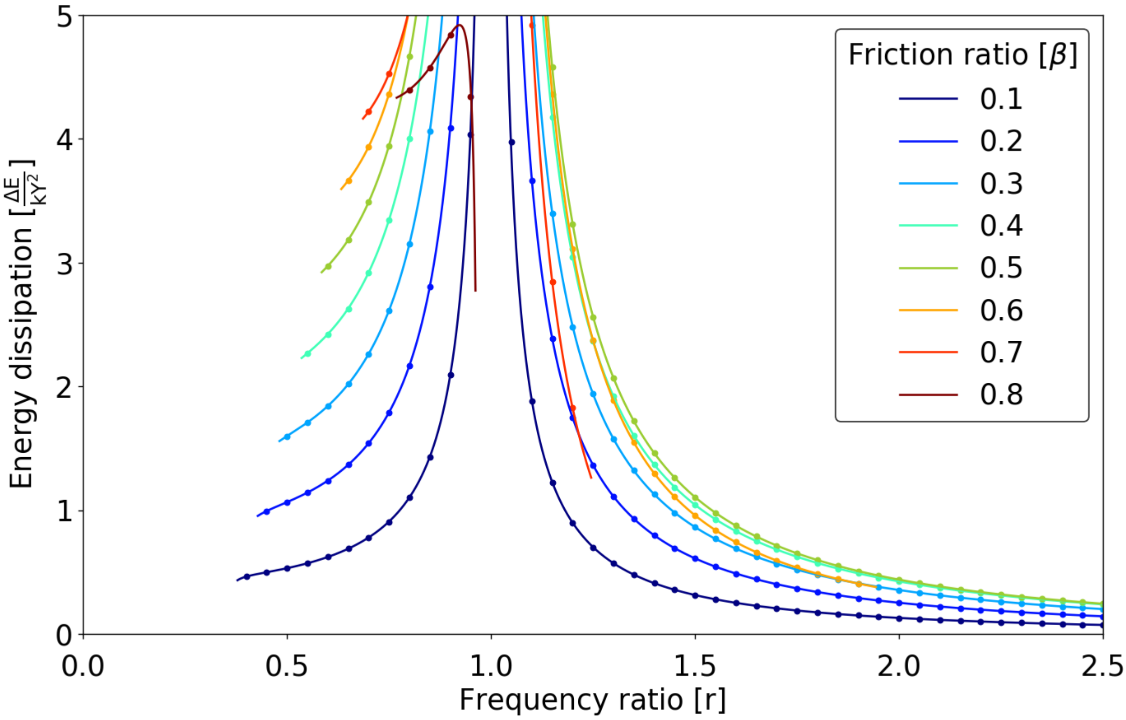

Figure 3.4: Numerical evaluation of dimensionless energy dissipation per cycle for the SDOF system with Coulomb friction contact for varying parameters r and β, continuous motion only: comparison between analytical method (round markers) and hysteresis method (continuous lines).

thus the resonance peak is located at a lower frequency than ω_n, where the excitation frequency equals ω_d. In the case of friction damping, the same shift occurs for high friction ratios. This can be seen for $\beta = 0.8$; its peak is located to the left of $r = 1$. A more in-depth comparison between the friction and viscous damped system will be carried out in Section 3.5.

- There is an inversion to the right of the resonance peak where higher friction ratios do not result in more energy being dissipated. $\beta = 0.5$ leads to the largest amount of energy being dissipated by friction per cycle for $r > 1$. Any further increase of the friction ratio brings about a reduction of energy dissipation. This inversion is a result of the curves shifting towards the left for high friction ratios, as explained above. The high frequency tails of the curves cross each other, causing the inversion.

- At high frequency ratios, that is $r > 1.5$, the difference in energy dissipation between the various curves shrinks. Increasing the friction force at high frequencies does not significantly enhance dissipation.

3.4.3. Energy dissipation continuous and stick-slip motion

To get a complete overview of the energy dissipation behaviour of the SDOF system with Coulomb friction, including the stick-slip motion regime, the hysteresis method is applied to calculate the energy dissipation of the numerical time response. The numerical simulations were carried out for values of r ranging from 0 to 2.5 and values of β ranging from 0.1 to 0.9. The obtained energy dissipation curves are shown in Figure 3.5.

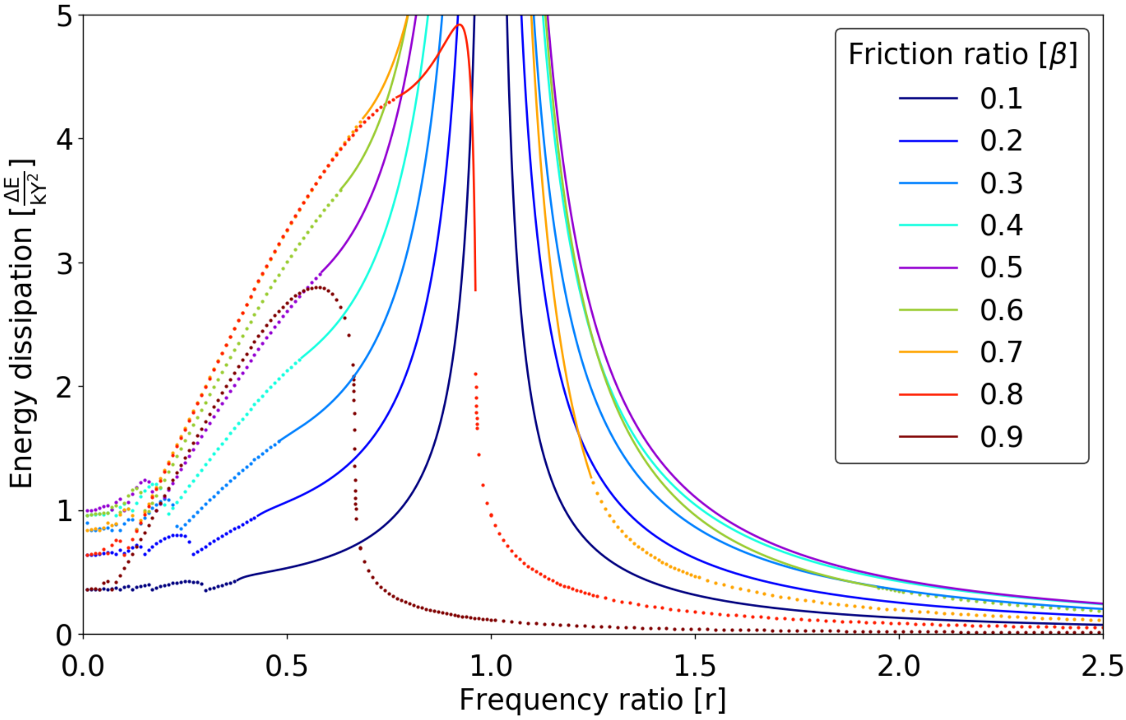

Figure 3.5: Dimensionless energy dissipation per cycle for the SDOF system with Coulomb friction contact for varying parameters r and β, based on numerical simulations: continuous motion (continuous lines) and stick-slip motion (round markers).

Each curve transitions smoothly from the stick-slip regime to the continuous regime and vice versa. The same characteristics listed under Figure 3.4 can be observed here as well, including the inversion and leftward shifts. New striking features of the plot are:

- Within the low frequency interval $0 < r < 0.3$ in the stick-slip motion regime, wavy and bumpy patterns can be seen. Changes in the number of stops per cycle, due to merging and splitting of the sticking sections, causes this bumpy behaviour [9].
- The curve corresponding to $\beta = 0.9$ is moved considerably more towards the lower frequencies compared to the other curves.

- Between the bumpy stick-slip region and $r = 1$, changes in the slope of the energy dissipation curves are visible when the friction ratio rises. A bump develops, where the slope is rather steep at first, diminishes and then increases again.
- For higher friction cases, there are two stick-slip regions. These two regions are located at low and high frequencies, respectively.

3.5. Viscous damper validation and comparison

In this section, the hysteresis energy dissipation calculation method (Equation 2.18) is validated by applying it to a viscous damped SDOF system. Afterwards the energy dissipation performance and properties of the Coulomb friction damper can be compared to those of the more conventional viscous damper.

Apart from the viscous damper that replaces the friction contact, the harmonically excited SDOF system with viscous damping displayed in Figure 3.6 is equivalent to the SDOF system with Coulomb friction in Figure 2.2 that is the main focus of this thesis.

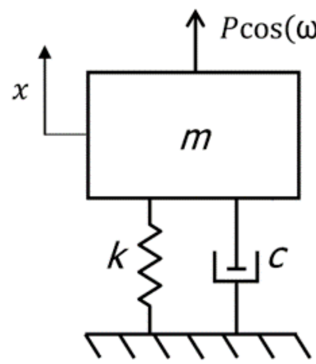

Figure 3.6: Harmonically excited SDOF system with viscous damping [2].

It is a mass-spring-dashpot system with mass m, spring stiffness k and damping coefficient c subjected to a harmonic load of frequency ω and amplitude P. The equation of motion of this system is:

$$m\ddot{x} + c\dot{x} + kx = P \cos \omega t \tag{3.4}$$

If we introduce the non-dimensional time τ from Equation 2.5 and the non-dimensional mass displacement $\bar{x}$ from Equation 2.6 and substitute them into Equation 3.4, the following dimensionless governing equation is obtained:

$$r^2\bar{x}'' + 2\zeta r\bar{x}' + \bar{x} = \cos\tau \tag{3.5}$$

With ζ being the damping ratio of the system, related to the damping coefficient according to the expression $c = 2\zeta m\omega_n$.

An analytical expression of the energy dissipated per cycle by the viscous damper in the mass-spring-dashpot system of Figure 3.6 is available in literature [24]:

$$\Delta E_{visc} = \int\limits_T c\dot{x}^2\, dt \tag{3.6}$$

With T representing one period and $\dot{x}$ representing the velocity of the mass. This formulation allows for a direct comparison to the hysteresis method. The expression can be made non-dimensional by inserting the non-dimensional time and displacement again and multiplying with k/P^2 (which is equivalent to the division by kY^2 in Equation 2.16):

$$\Delta\overline{E}_{visc} = 2\zeta r \int\limits_{2\pi} \bar{x}'^2\, d\tau \tag{3.7}$$

With 2π being the length of one dimensionless time period and $\bar{x}'$ representing the dimensionless mass velocity. Numerical simulations of the governing equation (Equation 3.5) are performed in order to get time response data on which the analytical energy dissipation formula from literature and the hysteresis method can be applied. The SDOF viscous damped system introduces no numerical stiffness, so events and stopping conditions are not necessary. The solve_ivp function from the Scipy package [21] is used again for the numerical integration, using the RK45 integration method. All initial conditions are set to zero and $N_{cyc} = 50$. The same frequency ratio range, 0 to 2.5, is considered, as well as ζ values ranging from 0.1 to 0.9. One steady-state cycle is used for the calculation of the energy dissipation. The computed energy dissipation curves of the viscous damped system are illustrated in Figure 3.7. The plot shows an exceptional agreement between the analytical formula from literature and the hysteresis method in the entire parameter space. The viscous damper analogy confirms the validity and usability of the hysteresis energy dissipation calculation method. Moreover, it can be seen that:

- When looking at the curves corresponding to higher damping ratios, their peaks are shifted gradually towards lower frequencies. This is due to the damped natural frequency of the system, as explained in Section 3.4.2. These shifts cause inversions of the curves.

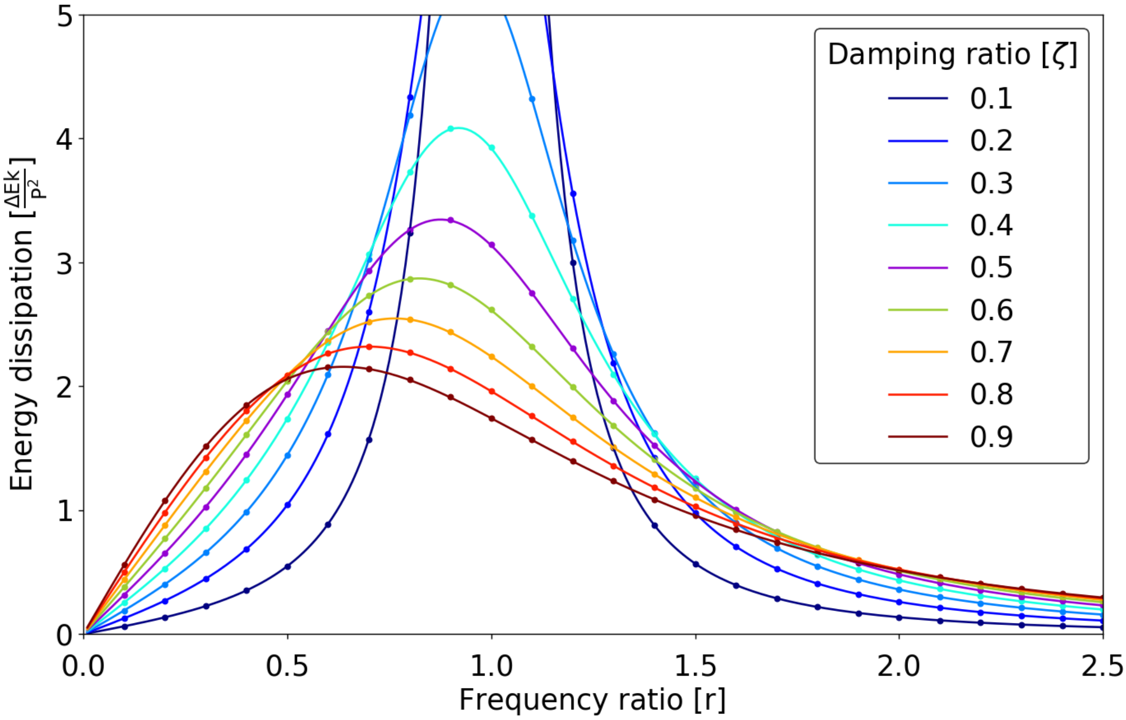

Figure 3.7: Dimensionless energy dissipation per cycle for the SDOF system with viscous damping for varying parameters r and ζ, based on numerical simulations: comparison between analytical formula from literature (continuous lines) and hysteresis method (round markers).

- There are two inversion regions where the vertical order of the various curves is reversed. For lower and higher values of the parameter r, a higher damping ratio ζ leads to more energy being dissipated per cycle. On the other hand, around $r = 1$, lowering the damping ratio increases the energy dissipation. Dai et al. also found these inversions in their study [13].

- Changing the damping ratio of the system does substantially alter the energy dissipation around the resonant frequency, whereas at the lower and high ends of the frequency range such a change results in a marginal alteration of the energy dissipation.

Taking into account Figure 3.7 and Figure 3.5, the energy dissipation properties of friction damped and viscous damped SDOF systems can be compared. One feature that both cases have in common is that with increasing damping or friction ratio, the peak of the respective dissipation curve moves to the left. Both friction and viscous damped systems have inversions because of the curves shifting towards lower frequencies.

Regarding the energy dissipation performance, the viscous damper is more effective at dissipating energy close to the resonance frequency and less effective at dissipating energy at low and high frequencies, given the curves being relatively close to each other in those regions. This is logical, since the energy dissipated by the viscous damper depends on the velocity, which is largest near resonance. The Coulomb friction contact also dissipates less energy in the high frequency region given the marginal differences between the curves. On the other hand, it is quite effective at dissipating energy at sub-resonant frequencies. The increase in dissipation between the curves at $r < 1$ for increasing friction forces in Figure 3.5 is evidence of this property. The work done by Dao et al. confirms these differences in energy dissipation performance between the friction and viscous cases [13].

3.6. Conclusion

The steady-state time response and energy dissipation performance of a SDOF Coulomb friction oscillator subjected to harmonic base excitation have been numerically analyzed in this chapter.

An algorithm has been implemented to calculate the dynamic time response of the SDOF system with Coulomb friction contact for any combination of the parameters r and β using numerical time integration. The numerical approach is event-driven so that certain events and conditions enable the simulation to smoothly transition from sticking to sliding phases and vice versa in the stick-slip motion regime. The complete time response of numerically stiff stick-slip motions is computed via piecewise integration of the sliding phases.

Regarding the steady-state time response, continuous motion and various stick-slip motions have been found. The different time responses are consistent with results from literature [8, 11]. In addition, an asymmetric non-sticking motion has been observed for parameters corresponding to another study [9].

Considering only the numerical solutions in the continuous motion regime, the energy dissipated by friction per cycle evaluated with the analytical method matches flawlessly with the energy dissipation evaluated with the hysteresis method. The hysteresis method properly shows the energy dissipation in the stick-slip regime, depicting bumpy behaviour for $r < 0.3$ due to the number of stops per cycle changing. When it comes to the energy dissipation metric, the main findings are:

1. Friction energy dissipation increases towards the resonance frequency, as to be expected. Increasing the friction force magnifies dissipation as well, until certain friction ratios. Higher friction mainly enhances the energy dissipation significantly for $r < 1$.

2. There is an inversion for $r > 1$; for these higher frequencies, increasing the friction ratio only amplifies the energy dissipation until a certain value of β has been reached. Further increasing β beyond this limit value decreases the energy dissipated by friction.

3. For relatively high friction forces, the energy dissipation curve is shifted towards lower frequencies due to the damped natural frequency of the system becoming lower.

The hysteresis method is validated by applying it to the numerical response of a harmonically excited SDOF mass-spring-dashpot system. The energy dissipation according to the hysteresis method is in excellent agreement with the results from the analytical formula available in literature [24]. Comparing the performance of friction and viscous damped systems, a viscous damper is more effective at dissipating energy near resonance, whereas a friction damper is better at dissipating energy in the frequency region below resonance.

All in all, the numerical results of this chapter help to better understand the friction behaviour and energy dissipation properties of the SDOF system with Coulomb friction. It has to be noted that these results are heavily reliant on assumptions and models, such as the relatively simple Coulomb friction law. Even though this may limit the validity of the numerical results, they are still useful grounds for the next chapter and can be compared to experimental results.

4

Experimental investigation of different contact materials

Contents

4.1. Introduction

This chapter presents an experimental investigation of the friction behaviour and energy dissipation performance of a SDOF system subjected to harmonic base excitation for three different contact materials. The goal of this investigation is to obtain the time response and energy dissipation of each contact material for varying excitation frequencies, friction forces and time scales in order to compare and understand the performance and characteristics of the materials. Secondly, this chapter aims to establish a link between the theoretical results from Chapter 3 and experimental observations to substantiate the findings of this research.

A single-storey shear frame is used to carry out the experiments. The considered contact configurations are steel-to-steel, rubber-to-steel and aramid-to-steel. To cover two different time scales, the investigation is split up into short-term and long-term experiments. Short-term and long-term results for the frictional behaviour and energy dissipation performance of the different materials are analyzed and compared to each other, as well as to the numerical results.

The procedure and test setup of the experimental investigation is explained in detail in Section 4.2. Section 4.3 presents the outcome of the short-term experiments regarding the friction behaviour and dissipation of the different materials, including a comparison to the numerical results. Subsequently, the long-term test results are shown and compared to the findings of the previous section in Section 4.4.

4.2. Experimental test setup and procedure

In this section, the test setup that is used to carry out the experiments of this research is presented. In addition, the chosen contact materials and the procedure of the experimental campaign are described as well.

4.2.1. Test apparatus

A single-storey shear frame that consists of two metal plates, one base plate and one top plate which are connected to each other with four metal stanchions, is used for the experimental campaign of this thesis. The setup is presented in Figure 4.1.

The steel disc that presses on the surface of the top plate initiates a friction force in the system through the line of contact between the plate and disc. The steel disc is connected to a rod with a steel fork. This fork allows the disc to rotate around the longitudinal axis of the rod so that the surface of the disc is pressed against the surface of the top plate as flat as possible, with no space in between. The pinned rod has brass weights attached to it and serves as a counterweight mechanism; by changing the position of the counterweights along the bar or adding or removing weights, the normal force and thus the friction force that the disc exerts on the top plate can be adjusted. The fixed wall configuration is considered by pinning the rod of the counterweight system to the external steel frame. The test rig is the same as the one Marino used in his experimental work [8], save for the disc and fork which are new. To better

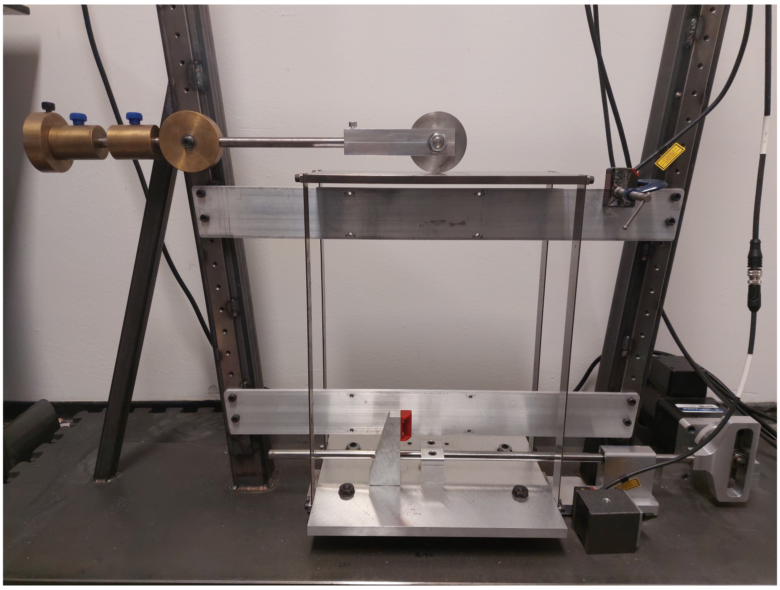

Figure 4.1: Photo of the test setup used for the experiments. The system can be harmonically excited through horizontal movement of the base plate, which is connected to an electric motor via a Scotch-yoke mechanism. A normal force is applied to the top plate by an externally fixed counterweight mechanism with a disc.

understand the test setup, a schematic representation from Marino [8] is shown in Figure 4.2.

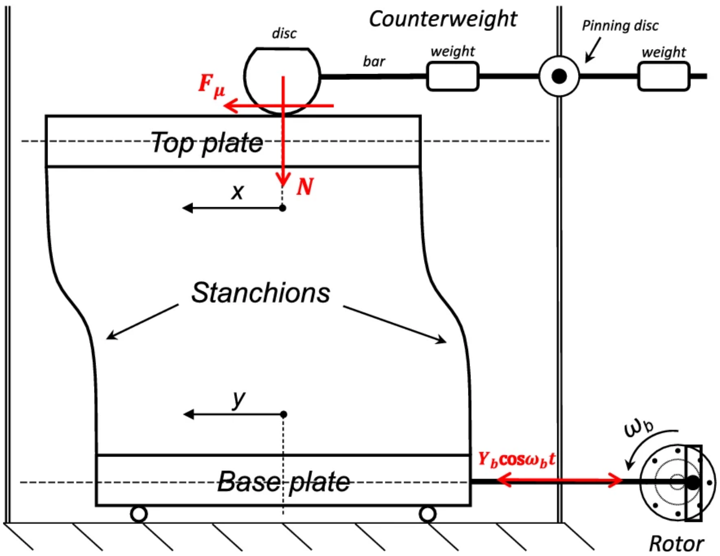

Figure 4.2: Schematic representation of the test rig according to Marino [8].

The rotation of the rotor (DKM-9PBK) is converted to the horizontal harmonic motion of the base plate through a Scotch-yoke mechanism, which excites the dynamic system. The rotation speed of the motor, and thus the excitation frequency of the base plate, can be regulated with an inverter motor speed regulator (RS Pro RS510). The amplitude of the base plate motion is fixed by not changing the location of the Scotch-yoke on the rotor. The displacements of both the top (mass displacement) and base plate (excitation) are measured during experiments by two laser displacement sensors (model optoNCDT 1420, measuring range up to 50 mm [25]), which are connected to the external steel frame.

It is worth mentioning that Marino verified that the single-storey steel frame used for the experimental investigation can be appropriately represented by a SDOF model [8]. This is essential because the numerical results are based on a SDOF model with Coulomb friction and it needs to be possible to compare them to the experimental results. The top plate represents the mass, the base plate represents the oscillating wall, the four stanchions represent the spring and the line of contact between the top plate and the disc is the friction contact.

4.2.2. Contact materials

The three contact materials that are investigated are steel, rubber and aramid. More specifically, the different friction contact configurations are steel-to-steel, rubber-to-steel and aramid-to steel. Steel acts as a baseline in each contact to enable proper comparison between the three materials.

The steel grade of the disc is S355 structural steel. Both the steel disc and steel top plate are polished. Steel was chosen because it is an easily available and abundant construction material. It is common in friction dampers and steel-to-steel is a very common combination for sliding and rolling contacts in engineering systems [26]. It is easily mountable since the contact can be created by letting the steel disc rest on the steel top plate.

The rubber used for experiments is a natural rubber (NR40 Luna Para rubber plate from ERIKS [27]). Rubber was chosen as a contact material because it is used in many technical applications where large frictional forces occur, such as rollers and laminated isolation bearings [28]. It is flexible under lateral forces; this could introduce a lag effect in the time response. An interesting property of rubber friction is that energy is partially dissipated via internal friction of the rubber particles [29]. Hard rubbers in particular have a relatively high energy dissipation capacity and abrasion resistance [12]. A flat rubber strip is mounted to the surface of the top plate with double-sided tap, see Figure 4.3. The tape was chosen such that the adhesion is as strong as possible so that the connection can be considered rigid, while still making removal of the tape possible. The steel disc of the counterweight rod is put on top of the rubber strip to create the frictional contact.

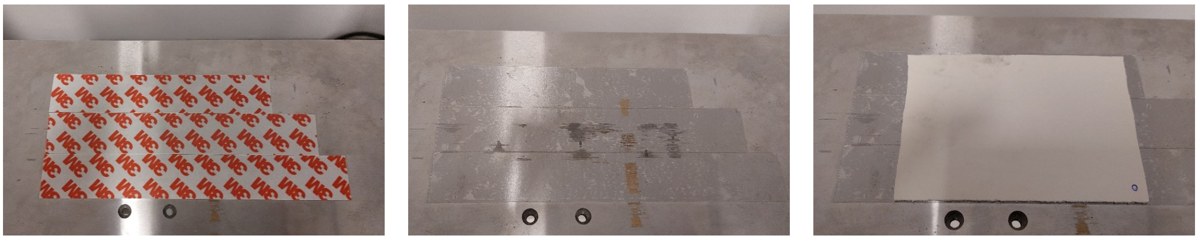

(a) Fixing double-sided tape **(b)** Peeling of tape seal **(c)** Attaching rubber strip

Figure 4.3: Mounting the rubber strip on the surface of the steel top plate.

The third contact material, aramid, is a woven material of synthetic fibres commonly used in (automotive) brake-line pads. Because of their technological significance, it is suggested by Cabboi that brake-line materials are studied in friction related research [30]. Similarly to the rubber case in Figure 4.3, a strip of aramid is attached to the top plate with double-sided tape and the steel disc rests on this strip.

4.2.3. Test procedure

The experimental campaign is split up into two parts: short-term and long-term experiments. Short-term tests are carried out to achieve a large parameter space of various frequency ratios and friction forces. The goal of the long-term tests is to capture long-term effects and the variation of the material performance over time.

The short-term experiments cover frequency ratios from $r = 0.05$ to $r = 2.5$, skipping a frequency band near resonance to avoid damage to the test rig due to excessive response amplitudes. At higher frequencies, the frequency step size between different measurements is increased because based on the numerical results and observations during tests, not much is changing in this region. The friction force is changed by altering the counterweight mechanism. Since the friction force cannot be measured directly, the weight of the disc on the material underneath is measured with a scale. Measuring the disc weight is equivalent to measuring the normal force exerted by the disc. For each material, five normal forces are considered. For aramid and steel normal forces of 1.0 N, 1.25 N, 1.5 N, 2.35 N and 3.2 N are used, and for rubber normal forces of 0.5 N, 0.75 N, 1.0 N, 1.25 N and 1.5 N. The rubber normal forces are lower because for 2.35 N and 3.2 N the mass got stuck before the end of the test, but a set of five different normal forces was still desired. Each short-term test lasts 90 seconds, starting with turning on the harmonic excitation and thus including the transient.

The long-term experiments last 30 minutes each, including the transient. Since these time frames are quite long, only one normal force of 1.25 N is considered. One lower frequency of $r = 0.3$ and one higher frequency of $r = 1.2$ are investigated, so that both continuous and stick-slip motions can be observed for a long duration. Fewer parameter values are required to limit the execution time of the experiments.

The surfaces of the contact materials and the steel disc are carefully cleaned after each test to remove debris.

4.2.4. Post-processing measurements

After performing the experiments and acquiring the signals, consisting of the mass motion x (top plate displacement vector vs. time vector) and base motion y (base plate displacement vector vs. time vector), the signals need to be post-processed in order to be able to evaluate the desired metrics regarding energy dissipation and frictional behaviour.

The natural and driving frequencies are necessary to estimate the frequency ratio of each test (Equation 2.7). The (angular) driving frequency ω can be changed by adjusting the input frequency of the inverter. ω can be found by computing the FFT (Fast Fourier Transform) of the base motion and analyzing its frequency spectrum. The peak of this spectrum is located at the driving frequency $f = \frac{\omega}{2\pi}$. To obtain the natural frequency of the test rig, free vibration of the mass is induced by displacing the top plate and letting it freely vibrate. Subsequently, the FFT of the mass motion is computed and the peak of its frequency spectrum is positioned at the natural frequency. This has been done several times and averaging the results gives $f_n = \frac{\omega_n}{2\pi} = 3.126$ Hz. By using the FFT and frequency spectra, the frequency ratio of each test can be estimated. To make the peaks in the frequency spectra more accurate, zero-padding and the Hanning window are used to process the signals to reduce spectral leakage and increase the frequency resolution [31].

The mass motion x and base motion y need to be made non-dimensional in order to compare them to numerical results and to be able to apply the hysteresis method to compute the non-dimensional energy dissipation. x and y are made dimensionless by dividing them by the amplitude of the base motion Y (Equation 2.6, replacing P with kY^2 gives a division by Y). Non-dimensional time is obtained by multiplying the time vector t with the driving frequency ω (Equation 2.5).

4.3. Short-term experiments

After performing the short-term experiments for the frequency ratios and normal forces mentioned in Section 4.2.3, the friction behaviour and energy dissipation properties of the materials can be examined. The friction behaviour can be analyzed by looking at the time response of the mass (mass motion), whereas the energy dissipation performance can be studied after applying the hysteresis method to one cycle of steady-state motion. The first 20 seconds of the time response have been cut off to skip the transient.

4.3.1. Friction behaviour

For all three materials, continuous as well as multiple stick-slip motions have been seen. The rubber and aramid stick-slip responses have no more than two stops per cycle, while stick-slip responses with more than two stops per cycle do occur for the steel-to-steel contact. This interesting difference in friction behaviour could be important for identifying the underlying friction law of the sliding contacts. Cabboi et al. compared the Coulomb friction law to the rate-and-state Dieterich-Ruina friction law and found that for $r = 0.1$, $\mu_s \geq \mu_k$ and certain parameters of the rate-and-state model, the Dieterich-Ruina law is unable to achieve intermediate stops, leading to a stick-slip motion with two stops. The Coulomb law on the other hand is able to produce a multiple stops stick-slip motion for similar parameters [32]. Looking at the experimental stick-slip responses, this might suggest that the friction behaviour of aramid and rubber is better described by the rate-and-state Dieterich-Ruina friction law than the Coulomb friction law and vice versa for steel. The numerical results reinforce the suggestion that the Coulomb model is more suitable for steel than for aramid and rubber, since Figure 3.2 also shows stick-slip motions with more than two stops per cycle. Nonetheless, this inverse approach of friction law identification needs to be used with caution because mistakes are easily made.

Furthermore, the beating phenomenon has been observed for low friction cases and near the resonant frequency. Examples of steady experimental time responses can be seen in Figure 4.4a and 4.4b. Unsteady signals have also been observed however, see Figure 4.4c and 4.4d for examples.

Friction is a highly complex physical process with lots of factors influencing its behaviour, as opposed to the friction models and numerical simulations that simplify it. Because of

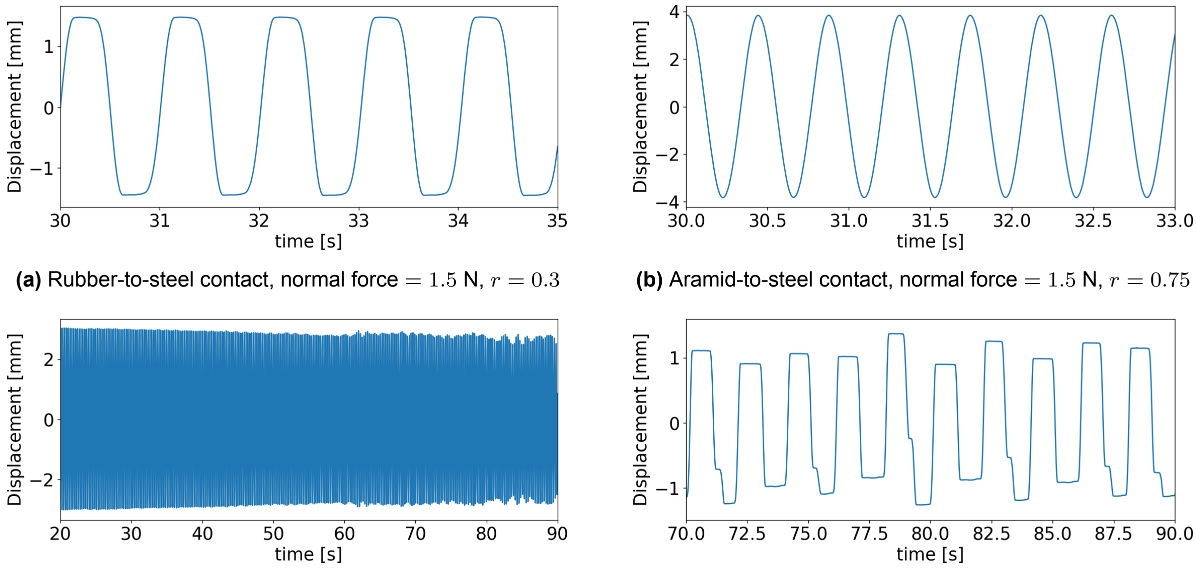

(a) Rubber-to-steel contact, normal force $= 1.5$ N, $r = 0.3$

(b) Aramid-to-steel contact, normal force $= 1.5$ N, $r = 0.75$

(c) Steel-to-steel contact, normal force $= 1.5$ N, $r = 1.25$

(d) Steel-to-steel contact, normal force $= 2.35$ N, $r = 0.15$

Figure 4.4: Examples of steady **(a,b)** and unsteady **(c,d)** experimental time responses.

this, unsteady and irregular experimental responses are expected. When comparing the experimental and numerical responses, Figure 4.4a and 4.4b are similar in shape to Figure 3.2c and 3.2a, respectively. Other steady experimental responses also correspond well with numerical results. On the other hand, unsteady motions such as Figure 4.4c and 4.4d are very different from the numerical solutions in Figure 3.2. This implies that the Coulomb friction model is suitable for describing regular motions, but cannot capture unsteady friction behaviour.

To quantify the irregularity of the frictional behaviour and to gain insight into how frequency and friction force affect this irregularity, the so-called irregularity index has been developed. The irregularity index of a signal is evaluated as:

$$\frac{1}{N_{cyc}-1}\sum_{j=1}^{N_{cyc}-1}\left(\frac{\sum_{i=1}^{N_p}|x_{j+1,i}-x_{j,i}|}{\sum_{i=1}^{N_p}|x_{j,i}|}\right) \tag{4.1}$$

With N_{cyc} the number of cycles and N_p the number of data points in one cycle. This index measures the irregularity of the time response. It is the averaged normalized difference between the points of one cycle and the points of a subsequent cycle for the entire signal. The higher the irregularity index, the more irregular the experimental time response is. The irregularity index of every short-term experiment has been calculated and is visualized in a color plot in Figure 4.5. The limit value of the color scale is the maximum occurring irregularity index minus 0.1 to increase the contrast between the other colors and magnify the differences for clarity. When looking at the color plot of the irregularity index, several things can be noted:

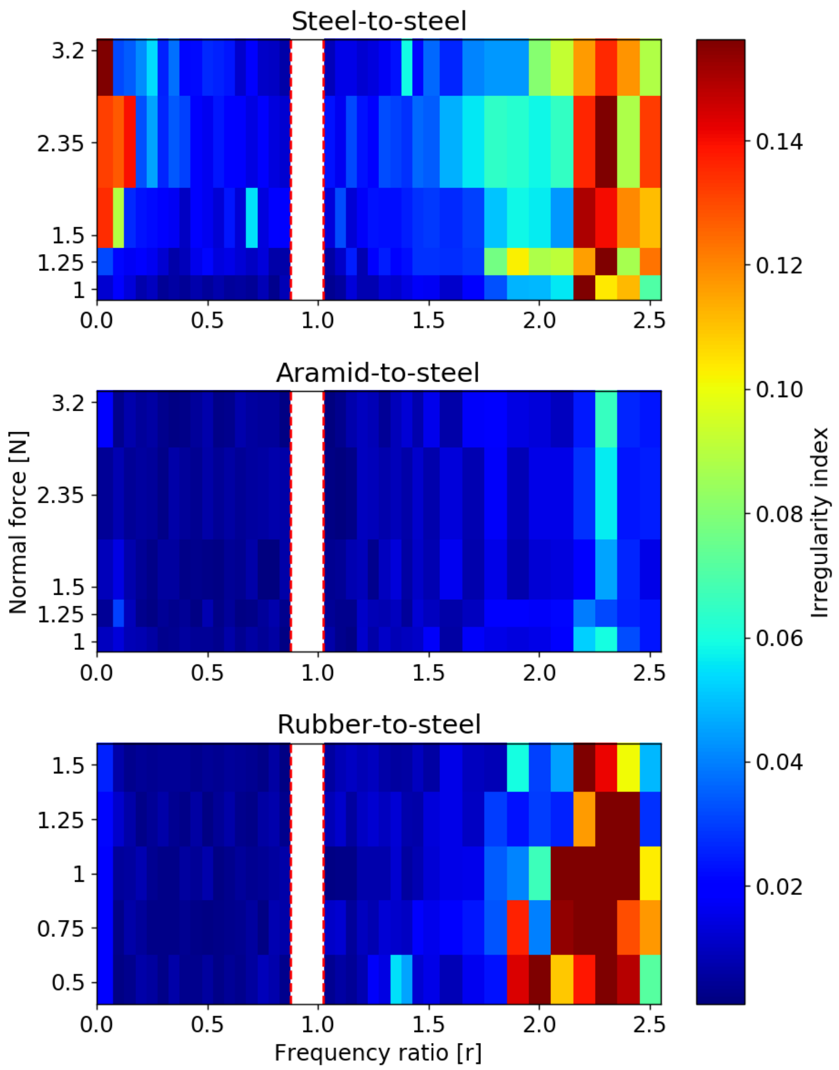

Figure 4.5: Irregularity index of the short-term experiments of all three contact materials. Frequencies near resonance have been skipped, hence the white space and red dotted lines.

- Higher normal forces and thus higher friction forces generally cause the experimental time response to be more unsteady, especially for the steel-to-steel contact.
- Higher values of r also increase the irregularity index, $r = 2.3$ in particular. However, this irregularity is mainly attributed to the base excitation, which is less harmonic at high frequencies due to the fast rotation speed of the motor.
- Some stick-slip behaviour of the steel-to-steel contact is quite unsteady for $r \leq 0.15$ and normal forces $\geq$ 1.5 N. Figure 4.6 shows an example of this irregular stick-slip motion.

- The frictional behaviour of aramid is very regular and constant.
- The time response of the rubber contact is very irregular in the high frequency region, but this is partially due to vertical bouncing of the steel disc on the rubber strip at relatively low normal forces (or disc weights).

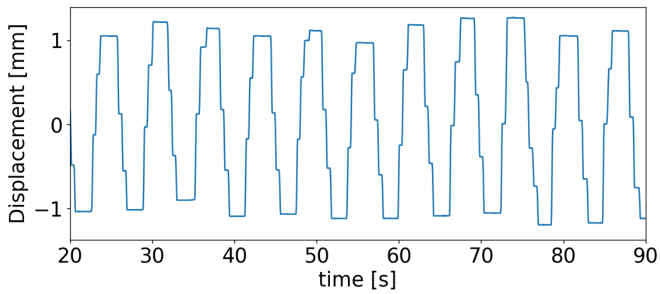

Figure 4.6: Irregular multiple-stops stick-slip motion of the steel-to-steel contact for $r = 0.05$ and normal force $= 1.5$ N. The number of stops per cycle and the amplitude are changing.

Material properties that influence the irregularity of the response are the coefficient of friction and resistance to abrasion. This is because the friction coefficient is directly related to the friction force. Moreover, a wear resistant contact material tends to show regular behaviour since its surface is not altered during sliding. Figure 4.5 implies that aramid has a low friction coefficient and high resistance to wear, for steel and rubber it is the opposite. The low friction coefficient of aramid is also found in other studies [33–35].

Regarding the frictional behaviour of the rubber-to-steel contact, interesting bumps and tilted peaks in the experimental response have been observed. These characteristics are depicted in Figure 4.7.

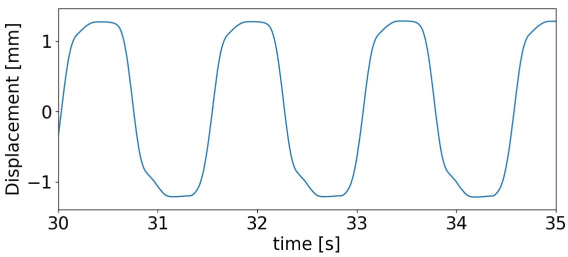

(a) Normal force $= 1.5$ N, $r = 0.2$

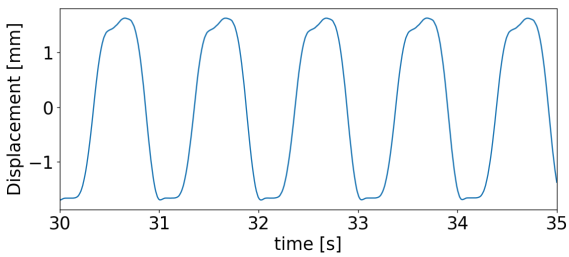

(b) Normal force $= 0.5$ N, $r = 0.3$

Figure 4.7: Experimental time response of the mass for the rubber-to-steel contact.

These peaks and bumps could be a result of the elasticity of the rubber which causes a lag effect. Due to the elasticity of the rubber the top of the strip can move slightly with respect to the bottom, so when the motion of the steel disc changes direction, the rubber strip causes the steel top plate to lag behind the disc movement. Overall, the short-term frictional behaviour of rubber is quite consistent.

4.3.2. Energy dissipation performance

The dimensionless energy dissipated by friction per cycle for each contact material is plotted in Figures 4.8, 4.9 and 4.10 for varying normal forces and frequency ratios. The last steady-state cycle of the 90 second time response of the mass is used to evaluate the energy dissipation of the rubber and aramid cases according to the hysteresis method. To make the energy dissipation curves of the steel-to-steel contact slightly smoother, the hysteresis method is not applied to the last cycle but to each full cycle in the last 15 second time frame instead, averaging the result. For the rubber and aramid this averaging did not change the results so for the sake of simplicity the last cycle is considered.

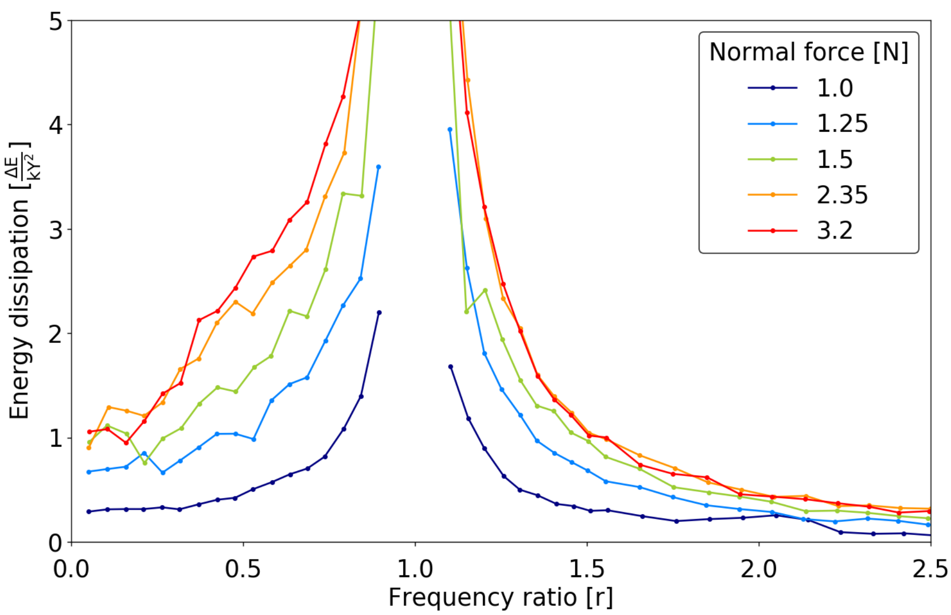

Figure 4.8: Dimensionless energy dissipation per cycle for the steel-to-steel contact for varying values of r and normal force, based on short-term experimental results.

When looking at the curves of the materials it can be noted that the energy dissipation enhances near resonance and is proportional to the normal force. This is expected, since a higher normal force results in a higher friction force. None of the energy dissipation plots display the distinct bumpy behaviour in the stick-slip motion regime of the numerical dissipation curves in Figure 3.5. It is apparently difficult to capture these bumpy patterns experimentally. It is also worth mentioning that the values of the experimental energy dissipation and the dissipation curve shapes are generally in good agreement with numerical results across the whole parameter space.

For the steel-to-steel contact, increasing the normal forces only increases the energy being dissipated by friction up until a certain point. This is evident by the fact that the differences between subsequent curves become smaller with higher normal force, especially at higher frequencies. The orange and red curves, corresponding to a normal force of 2.35 N and 3.2 N respectively, are even reasonably similar. The numerical results in Figure 3.4 and 3.5 illustrate the same feature of the dissipation curves getting closer to each other. This suggests that the experimental curves shift leftward with higher friction due to the damped natural frequency, just as the numerical curves. Additionally, The curves become less smooth as friction rises. Finally, the bump in the curves at frequencies below resonance observed for the numerical results appears to develop here as well.

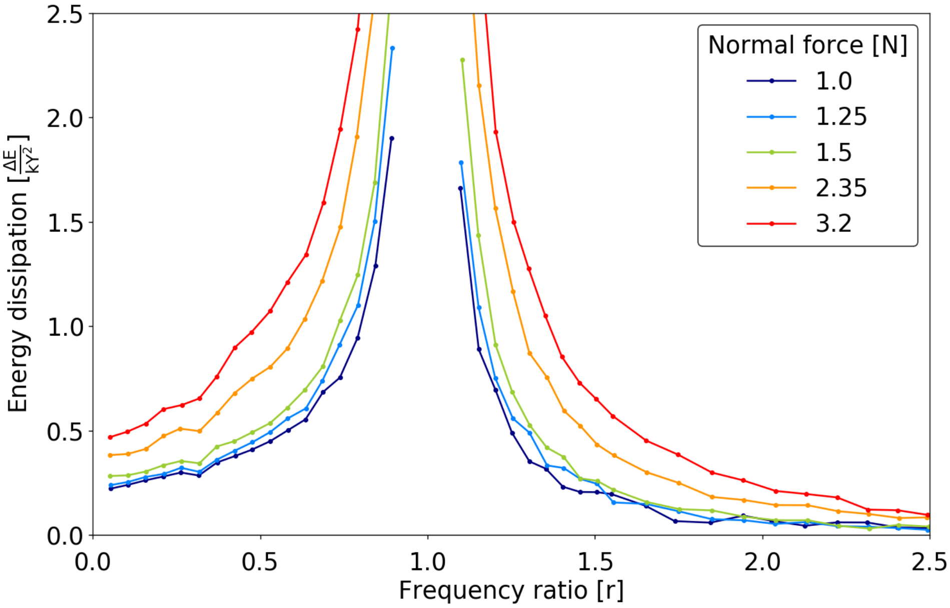

Figure 4.9: Dimensionless energy dissipation per cycle for the aramid-to-steel contact for varying values of r and normal force, based on short-term experimental results.

Considering the energy dissipation plot for aramid in Figure 4.9, it can be seen that the energy dissipated per cycle for the three lowest normal forces is almost identical for all values of r. Nonetheless, the energy dissipation performance is enhanced when further increasing the normal force to 2.35 N and 3.2 N. The lines in the graph are also quite continuous, in line with the consistent frictional behaviour of the aramid-to-steel contact discussed in the previous section.

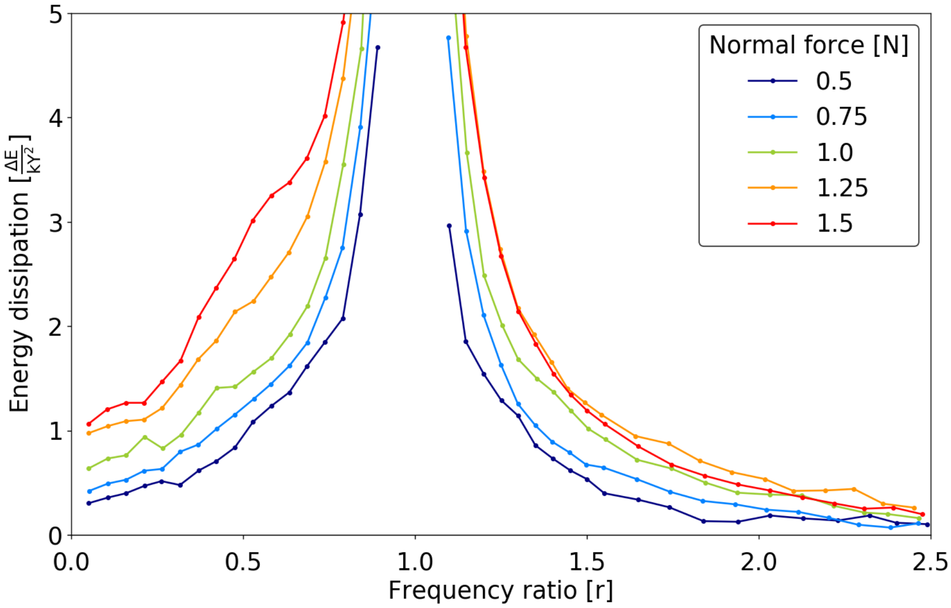

Figure 4.10: Dimensionless energy dissipation per cycle for the rubber-to-steel contact for varying values of r and normal force, based on short-term experimental results.

The energy dissipated by friction for the rubber-to-steel contact keeps increasing in the frequency region below resonance when amplifying the normal force. When looking at the right side of the resonance peak however, the differences between subsequent curves diminish with higher normal force, similarly to the steel-to-steel contact. This is evident from the orange and red curves in Figure 4.10, which are fairly identical. Furthermore, the red curve depicts the same bump to the left of the resonance peak as the numerical energy dissipation results in Figure 3.5.

A final comparison between the experimental energy dissipation performance of the three different contact materials is made in Figure 4.11, based on the normal forces they have in common. When looking at these graphs, the contact material with the best energy dissipation performance is rubber, followed by steel and then aramid. Since the kinetic friction coefficient is the predominant material property that affects energy dissipation (since energy is only dissipated by friction during the sliding phase [32]), the performance comparison suggests that rubber has relatively the highest kinetic friction coefficient, followed by steel and aramid. The energy dissipation of rubber is augmented due to its viscous material properties and internal friction [29]. Work done by Latour et al. shows that the friction behaviour of a hard-rubber-to-steel contact is stable, while the behaviour of a steel-to-steel contact is unstable. The energy dissipation capacity of the hard-rubber-to-steel contact is quite high [12]. The obtained

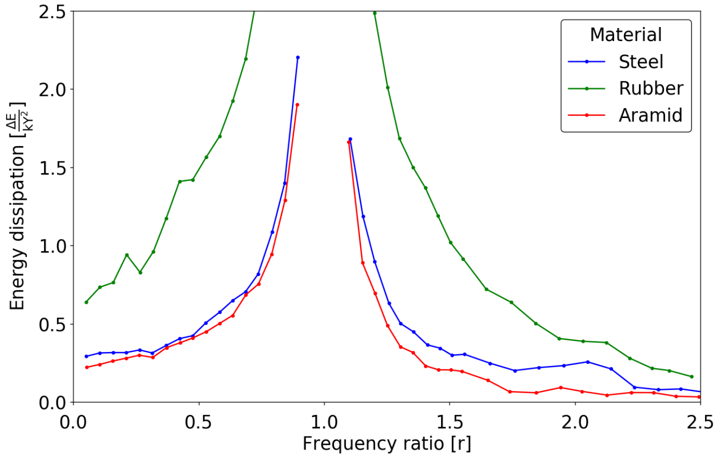

(a) Normal force $= 1.0$ N

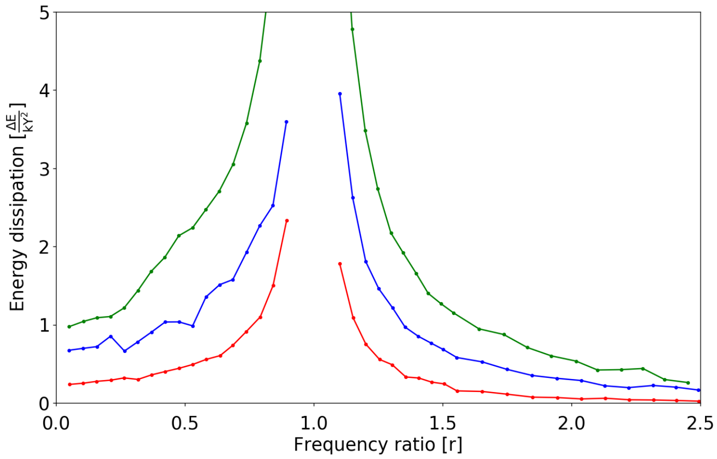

(b) Normal force $= 1.25$ N

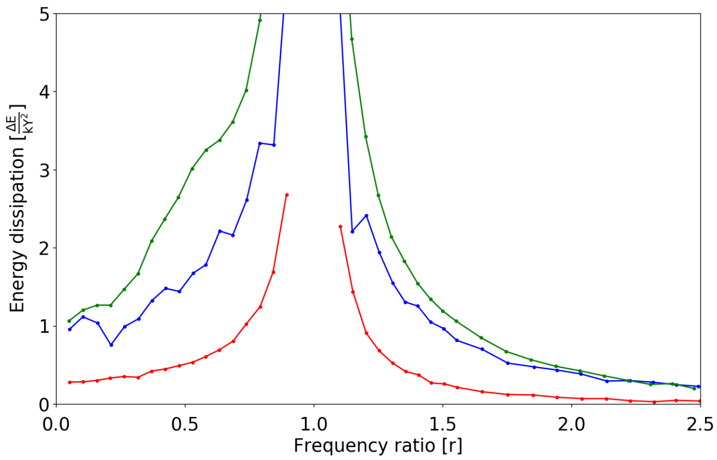

(c) Normal force $= 1.5$ N

Figure 4.11: Comparison between the energy dissipation performance of the steel-to-steel, aramid-to-steel and rubber-to-steel contact for different normal forces, based on short-term experimental results.

experimental results match fairly well with this study.

4.4. Long-term experiments

The frictional behaviour and energy dissipation ability of the different contact materials is also investigated based on long-term experiments to take their long-term performance into consideration. The hysteresis method is used again to compute the non-dimensional friction energy dissipation per steady-state cycle. The transient phase is skipped by deleting the first 20 seconds of the time response.

4.4.1. Debris and wear

A factor of great importance to the long-term performance of the friction contact materials is wear and the formation of debris. Because of the constant sliding under friction, the surface of the contact materials can degrade and wear down and debris can form due to material being scraped off the surface. Figure 4.12 presents the line of contact between the disc and the friction material after a long-term experiment to show possible wear and debris.

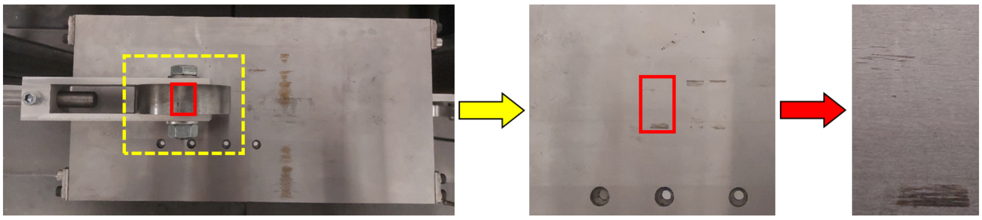

(a) Steel-to-steel contact

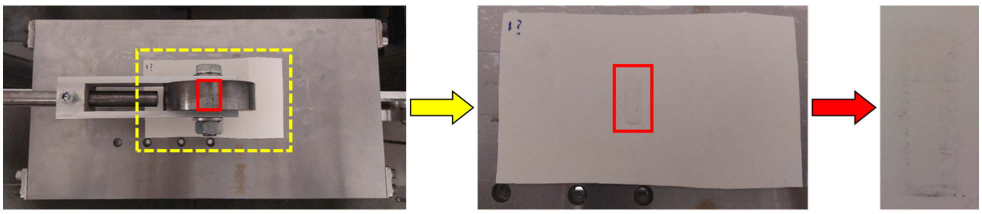

(b) Rubber-to-steel contact

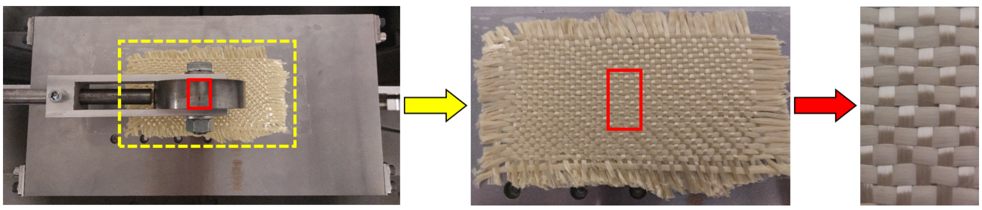

(c) Aramid-to-steel contact

Figure 4.12: Pictures of the frictional contact in the test rig for the different materials after performing a long-term test. First the yellow area is zoomed in on, then the red area, which is the line of contact between the steel disc and the material below.

Wear in the form of scratches at the bottom of the line of contact can be seen for the steel-to-steel case. This is due to the alignment between the surfaces of the steel disc and top plate, which is never perfectly flat in practice but slightly tilted. This causes scratches on the side of the top plate that is closer to the disc. Even though this is a limitation of the test setup for the long-term experiments, the experimental results of the steel contact should not be disregarded. Measured time responses are reasonably steady and comparable to the responses of other contact materials. Moreover, the steel-to-steel line of contact was initiated with extra care, after proper cleaning of the surfaces. Excessive wear of steel after cyclic loading is also found in reference [6].

Rubber and aramid on the other hand are more flexible and soft, allowing for a more flat alignment between the steel disc and the contact material. The rubber strip shows a black print that outlines the line of contact. This shape is caused by wear and the pressure of the disc. Some rubber debris, similar to the material coming off a pencil eraser when you use it, is also visible. The aramid strip shows no signs of abrasion at all.

4.4.2. Friction behaviour

Two frequency ratios ($r = 0.3$ for the stick-slip motion regime, $r = 1.2$ for the continuous motion regime) and one normal force of 1.25 N are considered for this part of the experimental campaign, resulting in two 30 minute time responses per contact material. The most noticeable characteristics of the observed long-term frictional behaviour of the different contact configurations are presented in Figure 4.13.

The complete long-term asymmetric time response of the steel-to-steel contact, depicted in Figure 4.13b, shows a highly variable motion. The steady-state solution appears to be multi-stable, meaning that multiple stable solutions exist. The exact origin of these multi-stable solutions is unknown, but physical agents of the friction process cause the time response to switch between these solutions. These switches are visible at the start of the signal in Figure 4.13b; the amplitude of the asymmetric displacement alternates from the positive to the negative vertical axis. Figure 4.13a illustrates the motion for $r = 0.3$ on a shorter time scale, displaying random bumps and secondary stops.

It has been found that the amount of stops per cycle for the stick-slip motion of the rubber-to-steel and steel-to-steel contact changes during the test. The rubber time response shows several irregular peaks and stops in Figure 4.13c and has a fluctuating amplitude in Figure

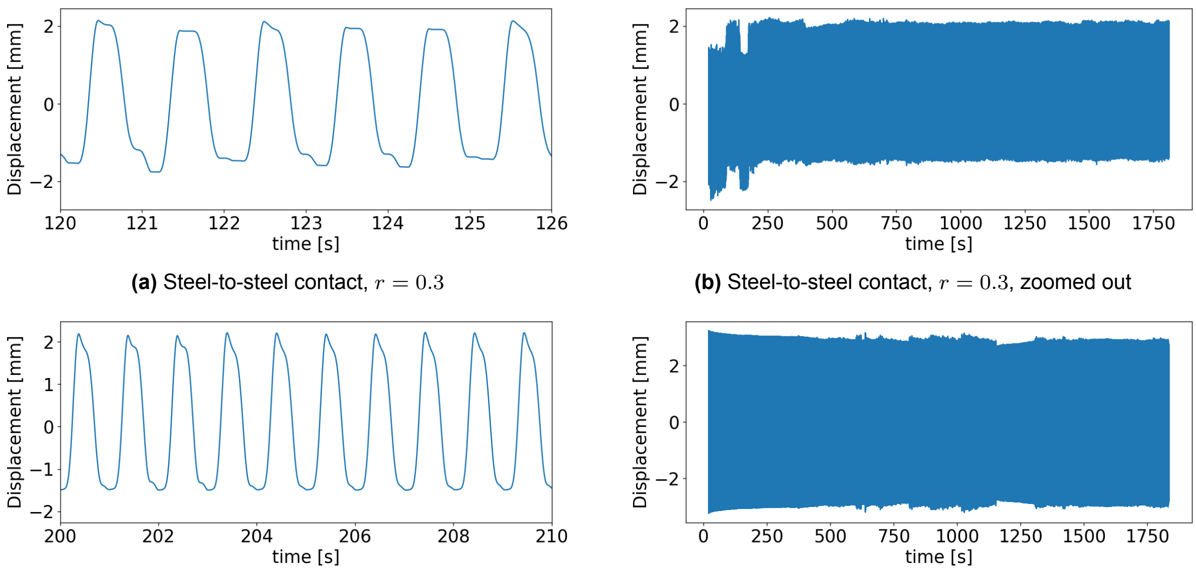

(a) Steel-to-steel contact, $r = 0.3$

(b) Steel-to-steel contact, $r = 0.3$, zoomed out

(c) Rubber-to-steel contact, $r = 0.3$

(d) Rubber-to-steel contact, $r = 1.2$

Figure 4.13: Examples of long-term experimental time responses for normal force $= 1.25$ N.

4.13d. In contrast, the observed long-term time response of aramid is very stable and regular.

The long-term time responses for $r = 1.2$ correspond generally well with the short-term and numerical responses, as well as the aramid response for $r = 0.3$. In contrast, the long-term friction behaviour of steel and rubber is very different and more irregular, especially the stick-slip motion. This difference in regularity of the friction behaviour is caused by various long-term effects, such as abrasion and debris formation.

4.4.3. Energy dissipation performance

The non-dimensional friction energy dissipation per cycle during the long-term experiments for the three materials is visualized in Figure 4.14 and 4.15, for stick-slip motion and continuous motion respectively. These plots show how the energy dissipation performance of the different contact materials changes over time. The energy dissipation of one cycle of the long-term response is computed with the hysteresis method, with a ten second interval between each analyzed cycle.

When looking at the long-term energy dissipation in Figure 4.14 and 4.15, it can be seen that the performance of steel and rubber is quite inconstant, whereas the performance of aramid is consistent. This distinction in consistency is in line with the friction behaviour results discussed in Section 4.4.2.

The long-term performance of aramid for $r = 0.3$ in Figure 4.14 shows a constant trend, the

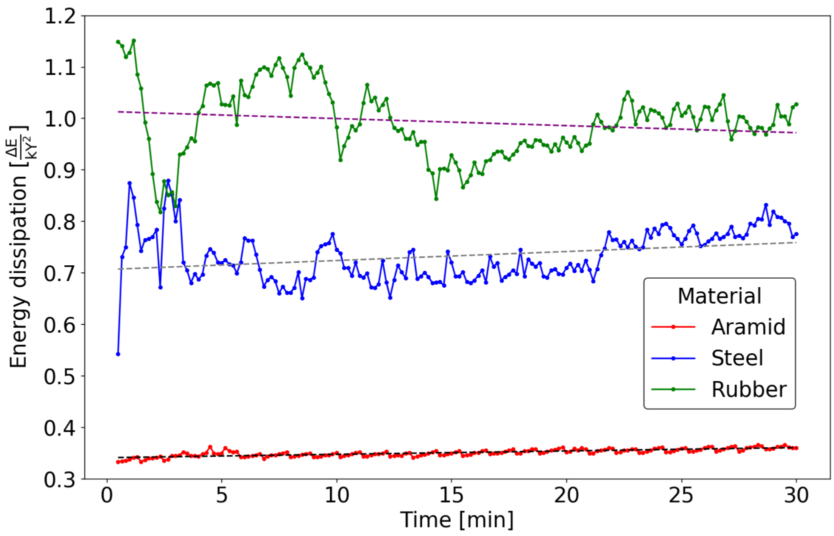

Figure 4.14: Dimensionless energy dissipation per cycle for the different contact materials for $r = 0.3$ and normal force $= 1.25$ N, based on long-term experimental results. Dotted trend lines are included.

steel energy dissipation trend slightly increases and the rubber trend line slightly decreases. Apart from the short-term energy dissipation of rubber being marginally larger, the long-term dissipation values illustrated in Figure 4.14 are overall in good agreement with the short-term experimental results.

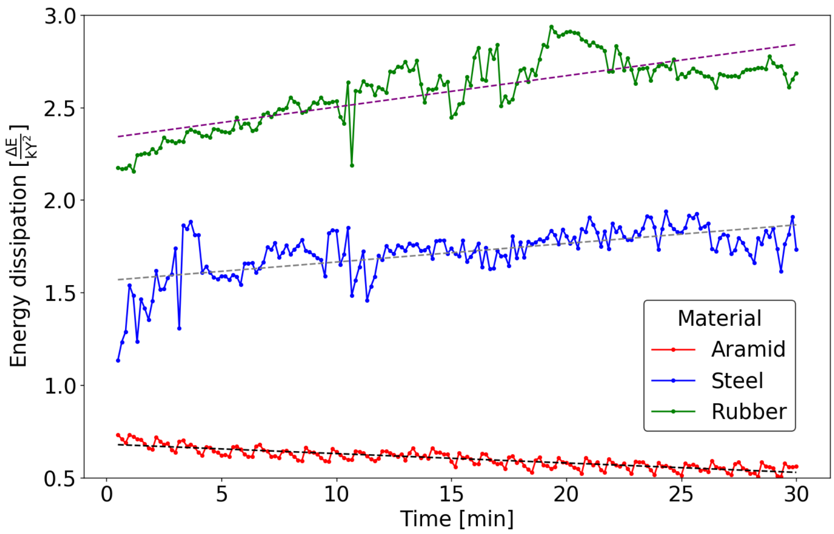

Figure 4.15: Dimensionless energy dissipation per cycle for the different contact materials for $r = 1.2$ and normal force $= 1.25$ N, based on long-term experimental results. Dotted trend lines are included.

In Figure 4.15, the long-term performance for continuous motion of aramid displays a slightly decreasing trend, steel has an increasing trend line and the rubber dissipation trend increases even more. The long-term energy dissipation results reported in Figure 4.15 concur with the short-term experimental results.

Finally, it is interesting to hypothesize on the long-term effects that influence the performance and how they provoke the change in energy dissipation over time. Fan et al. show that contact surfaces can flatten or roughen due to wear, depending on sliding speed and contact pressure [36]. The increased surface roughness is caused by the formation of new asperities; micro peaks on the surface that enhance friction. However, the asperities can also be sheared and pulverized, forming debris that can fill the valleys between the asperities. This reduces the ploughing effect of the asperities. If enough debris fills the valleys and covers the contact area, a continuous friction film which acts as a lubricant is created. It is evident that wear and debris can either lead to a higher or lower friction coefficient, and this definitely plays an important role in the fluctuation of the energy dissipation seen in the plots.

4.5. Conclusion

In this chapter, the friction behaviour and energy dissipation performance of a harmonically base-excited SDOF system with friction contact have been experimentally investigated for various contact materials .

A single-storey frame test setup has been used to carry out the experiments. The system is excited through harmonic base excitation and the friction contact is initiated between the top plate and an externally fixed steel disc. The contact material can be changed by mounting a material strip on the top plate. The different contact configurations that are considered are: steel-to-steel, aramid-to-steel and rubber-to-steel. The limitation of the steel-to-steel contact regarding asymmetric wear has also been discussed, but this does not completely disprove the validity of the measurements and test rig. The experiments consist of short-term tests for different frequency ratios and friction forces and long-term tests for fewer parameter values. The response metrics that are analyzed, are: the steady-state time response, the irregularity index (only for the short-term experiments) and the energy dissipation per cycle.

For the short-term tests, it was found that rubber and aramid stick-slip responses have a maximum of two stops per cycle, whereas steel has multiple-stops motions. This might indicate that the Coulomb model fits the steel friction behaviour better than the rubber and aramid friction behaviour, at least in the stick-slip regime. The irregularity index illustrates that higher friction generally leads to a more irregular response. Additionally, the index reveals highly irregular behaviour of the steel-to-steel contact in a certain domain of the stick-slip regime. The short-term time response of rubber depicts features that could be a result of the elasticity and lag effect of rubber. For all contact materials, the energy dissipation enhances near resonance and is proportional to the friction force, as expected. It can be noticed that for steel and to a lesser degree for rubber, the increase in energy dissipation due to an increase in friction force diminishes at higher friction, similar to the numerical results for Coulomb friction. Lastly, a bump in the dissipation curves of steel and rubber in the low frequency region is visible for high normal forces. The numerical dissipation curves have the same bump for high friction ratios.

The long-term frictional behaviour of aramid is very constant, while the rubber and steel behaviour is quite irregular. Similar to the long-term time response of the materials, the long-term energy dissipation of aramid is quite consistent, whereas the performance of rubber and steel changes over time. There are several long-term effects which can affect friction and thus energy dissipation, such as wear and debris.

When comparing the short-term experimental, long-term experimental and numerical results to each other, it can be concluded that:

1. The Coulomb friction model can accurately describe steady experimental friction behaviour, but cannot capture unsteady motions. This is expected, since the model is relatively simple and does not incorporate the numerous physical agents that influence the dynamic friction behaviour in practice.

2. The short-term time responses are more irregular than the the numerical results, and the long-term time responses are even more irregular than the short-term ones. This is a result of the complexity of the physical friction process and the long-term effects, respectively.

3. Short-term, long-term and numerical results for energy dissipation by friction are in good agreement with each other.

The numerical and experimental findings presented in Chapter 3 and 4 provide insight into the performance of the different contact materials with respect to friction behaviour and energy dissipation and are essential to the main conclusions of this thesis presented in the following chapter.

5 Main conclusions

The goal of this thesis was to develop an understanding of how different contact materials affect the performance of a friction damper with respect to its frictional behaviour and energy dissipation capacity.

The SDOF system with Coulomb friction contact between the sliding mass and a fixed wall subjected to harmonic excitation was considered. Numerical approaches were used to investigate the frictional behaviour of the system and the energy dissipated by friction. An experimental investigation was performed to obtain the friction behaviour and energy dissipation for the different contact materials of (1) steel, (2) rubber and (3) aramid in the following contact configurations, respectively: a steel-to-steel contact, a rubber-to-steel contact and an aramid-to-steel contact. Short- and long-term experiments were carried out. The performance of the different contact materials was compared. Moreover, the experimental results were compared to the numerical results for validation.

The principal results of this thesis are reviewed below:

1. Energy dissipation calculation methods for SDOF friction damped systems were derived. The most important calculation method is the hysteresis method; since it only requires the base motion and time response of the mass, it is very useful for experiments.

2. Numerical results for the response and energy dissipation of the SDOF system with Coulomb friction contact subjected to harmonic excitation were attained for continuous and stick-slip motions. The dependency of the energy dissipation on friction force and excitation frequency was shown in graphs.

3. Short-term and long-term experimental results for the friction behaviour and energy dissipation performance of steel, rubber and aramid were presented. The irregularity index was also developed to quantify the irregularity of the short-term time responses. Short-term experimental results, long-term experimental results and numerical results were compared to each other. Short-term, long-term and numerical results for energy dissipation were found to be in good agreement with each other.

The main findings regarding the friction behaviour, energy dissipation and long-term performance of the different contact materials are, respectively:

1. **Friction behaviour.** The stick-slip responses of aramid and rubber have no more than two stops per cycle, while steel shows stick-slip motions with more than two stops. This might suggest that the Coulomb friction model describes the friction behaviour of steel better than the behaviour of rubber and aramid. Secondly, a specific region of the stick-slip motion regime of the steel-to-steel contact corresponds to highly irregular behaviour, based on the irregularity index. The rubber friction behaviour shows characteristics that could be attributed to the flexibility of rubber.

2. **Energy dissipation.** As expected, dissipation by friction enhances near resonance and is proportional to the friction force. However, this proportionality declines when higher friction is considered for the steel-to-steel contact and rubber-to-steel contact.

3. **Long-term performance.** Considering a longer time scale, the friction behaviour and energy dissipation of aramid is stable and consistent. On the other hand, the friction behaviour and energy dissipation of steel and rubber is irregular and inconsistent.

Finally, taking the experimental results and research questions into account, the different contact materials can be ranked relatively to each other based on three performance criteria (with number 1 performing the best etc.):

- **Energy dissipation:** (1) rubber, (2) steel, (3) aramid.
- **Friction behaviour consistency:** (1) aramid, (2) rubber, (3) steel.
- **Wear resistance:** (1) aramid, (2) rubber and steel.

A very important material property affecting performance and thus these rankings is the friction coefficient. The outcome of the experiments suggests that rubber has the highest friction coefficient, followed by steel and then aramid.

6 Recommendations

Although the findings of this thesis allow a better understanding of the effects of the investigated contact materials on the performance of friction damping, they are reliant on and limited by the assumptions made, equipment used and assumed models. Several limitations and factors of uncertainty are briefly discussed in this chapter. A limitation of the steel-to-steel contact regarding asymmetric abrasion has already been discussed in Section 4.4.1.

It is worth noting that probably not all asymmetries seen in the experimental responses are due to real friction induced asymmetries. The exact causes are unknown, but the observed asymmetries might be a result of irregularities in the friction contact or in the test setup itself.

Additionally, SDOF systems, which are used extensively in this research, are very simple models. They often cannot accurately describe the behaviour of more complex real-life structures [2]. This limits the usefulness of the thesis results to real-life applications.

Finally, since the motion of the top plate in the single-storey frame used for the experiments is not perfectly straight, it is highly likely that the plate moves in the out-of-plane or lateral direction as well (in the direction perpendicular to the length of the top plate). This out-of-plane motion was not measured during the tests. This is a limitation because it means that the test rig is less well represented by a SDOF system.

Interesting suggestions for future research on friction damping and contact materials are: investigating more and other contact materials, long-term experiments with more excitation frequencies and friction forces, using the base-wall configuration from references [2, 4], considering other friction models for the numerical results and applying different types of excitation.

References

[1] M. R. W. Brake. “The Mechanics of Jointed Structures: Recent Research and Open Challenges for Developing Predictive Models for Structural Dynamics”. In: The Mechanics of Jointed Structures: Recent Research and Open Challenges for Developing Predictive Models for Structural Dynamics. 2017, pp. 1–702.

[2] L. Marino. “Dynamic analysis of mechanical systems with Coulomb friction”. PhD thesis. University of Oxford, 2021.

[3] A. A. Ferri. “Friction damping and isolation systems”. In: *Journal of Vibration and Acoustics, Transactions of the ASME* 117 (1995), pp. 196–206.

[4] L. Marino, A. Cicirello, and D. A. Hills. “Displacement transmissibility of a Coulomb friction oscillator subject to joined base-wall motion”. In: *Nonlinear Dynamics* 98.4 (2019), pp. 2595–2612.

[5] S. Jaisee, F. Yue, and Y. H. Ooi. “A state-of-the-art review on passive friction dampers and their applications”. In: *Engineering Structures* 235 (2021).

[6] M. Anoushehei et al. “Empirical evaluation of cyclic behavior of rotational friction dampers with different metal pads”. In: *Scientia Iranica* 25.6A (2018), pp. 3021–3029.

[7] I. Lopez Arteaga and H. Nijmeijer. “Prediction and validation of the energy dissipation of a friction damper”. In: *Journal of Sound and Vibration* 328.4-5 (2009), pp. 396–410.

[8] L. Marino and A. Cicirello. “Experimental investigation of a single-degree-of-freedom system with Coulomb friction”. In: *Nonlinear Dynamics* 99.3 (2020), pp. 1781–1799.

[9] G. Csernák, G. Stépán, and S. W. Shaw. “Sub-harmonic resonant solutions of a harmonically excited dry friction oscillator”. In: *Nonlinear Dynamics* 50.1-2 (2007), pp. 93–109.

[10] G. Licskó and G. Csernák. “On the chaotic behaviour of a simple dry-friction oscillator”. In: *Mathematics and Computers in Simulation* 95 (2014), pp. 55–62.

[11] D. J. Riddoch, A. Cicirello, and D. A. Hills. “Response of a mass-spring system subject to Coulomb damping and harmonic base excitation”. In: *International Journal of Solids and Structures* 193-194 (2020), pp. 527–534.

[12] M. Latour, V. Piluso, and G. Rizzano. “Free from damage beam-to-column joints: Testing and design of DST connections with friction pads”. In: *Engineering Structures* 85 (2015), pp. 219–233.

[13] W. Dai, J. Yang, and M. Wiercigroch. “Vibration energy flow transmission in systems with Coulomb friction”. In: *International Journal of Mechanical Sciences* 214 (2022).

[14] E. Popova and V. L. Popov. “The research works of Coulomb and Amontons and generalized laws of friction”. In: *Friction* 3.2 (2015), pp. 183–190.

[15] A. J. Morin. “New friction experiments carried out at Metz in 1831-1833”. In: *Proc French R Acad Sci* 4.1 (1833), pp. 1–128.

[16] F. Marques et al. “A survey and comparison of several friction force models for dynamic analysis of multibody mechanical systems”. In: *Nonlinear Dynamics* 86.3 (2016), pp. 1407–1443.

[17] J. P. Den Hartog. "Forced vibrations with combined viscous and coulomb damping". In: *The London, Edinburgh, and Dublin Philosophical Magazine and Journal of Science* 9.59 (1930), pp. 801–817.

[18] JP Den Hartog. "Forced vibrations with combined Coulomb and viscous friction". In: *Trans. ASME APM* 53.9 (1931), pp. 107–115.

[19] S.S. Rao. *Mechanical Vibrations*. Sixth Edition. Hoboken: Pearson Education, Incorporated, 2017, pp. 332–336. ISBN: 9780134361307.

[20] Daniel S Stutts. "Equivalent viscous damping". In: *Missouri University of Sciences and Technology: Rolla, MO, USA* (2009).

[21] Pauli Virtanen et al. "SciPy 1.0: Fundamental Algorithms for Scientific Computing in Python". In: *Nature Methods* 17 (2020), pp. 261–272.

[22] Richard P Brent. *Algorithms for minimization without derivatives*. Courier Corporation, 2013.

[23] L. M. Gil-Martín et al. "Dynamic magnification factors of SDOF oscillators under harmonic loading". In: *Applied Mathematics Letters* 25.1 (2012), pp. 38–42.

[24] Marie Dillon Dahleh and William T. Thomson. "Vibration, Mechanical". In: *Encyclopedia of Physical Science and Technology (Third Edition)*. Ed. by Robert A. Meyers. Third Edition. New York: Academic Press, 2003, pp. 455–473. ISBN: 978-0-12-227410-7.

[25] Micro-Epsilon. *optoNCDT 1420 manual*. URL: `https://www.micro-epsilon.com/download/manuals/man--optoNCDT-1420--en.pdf`.

[26] A. Cabboi and J. Woodhouse. "Validation of a constitutive law for friction-induced vibration under different wear conditions". In: *Wear* 396-397 (2018), pp. 107–125.

[27] ERIKS. *ERIKS Rubber sheet NR 40 LUNA PARA*. URL: `https://shop.eriks.nl/en/rubber-products-rubber-sheets/rubber-sheet-nr-40-luna-para-pr-ec011270-0012/`.

[28] K. Nakano et al. "Investigation on Dynamic Response of Rubber in Frictional Contact". In: *Frontiers in Mechanical Engineering* 5 (2019).

[29] B. N. J. Persson. "On the theory of rubber friction". In: *Surface Science* 401.3 (1998), pp. 445–454.

[30] A. Cabboi and J. Woodhouse. "Identifying short-term variation of dynamic friction by means of its frequency response function". In: *Journal of Sound and Vibration* 472 (2020).

[31] A. Brandt. *Noise and Vibration Analysis: Signal Analysis and Experimental Procedures*. EBL-Schweitzer. Wiley, 2011. ISBN: 9780470978115. URL: `https://books.google.nl/books?id=-1DSxrlhL5sC`.

[32] A. Cabboi, L. Marino, and A. Cicirello. "A comparative study between Amontons–Coulomb and Dieterich–Ruina friction laws for the cyclic response of a single degree of freedom system". In: *European Journal of Mechanics, A/Solids* 96 (2022).

[33] B. J. Briscoe and F. Motamedi. "The ballistic impact characteristics of aramid fabrics: The influence of interface friction". In: *Wear* 158.1-2 (1992), pp. 229–247.

[34] E. D. LaBarre et al. "Effect of a carbon nanotube coating on friction and impact performance of Kevlar". In: *Journal of Materials Science* 50.16 (2015), pp. 5431–5442.

[35] M. P. Rao et al. "Modeling the effects of yarn material properties and friction on the ballistic impact of a plain-weave fabric". In: *Composite Structures* 89.4 (2009), pp. 556–566.

[36] S. Fan et al. “Effect of braking pressure and braking speed on the tribological properties of C/SiC aircraft brake materials”. In: *Composites Science and Technology* 70.6 (2010), pp. 959–965.